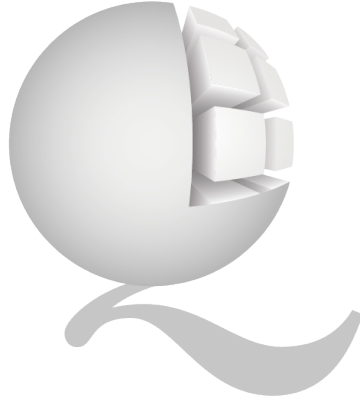


Horizon Europe Programme (2021-2027)  
EIC Pathfinder Open  
**HORIZON-EIC-2022-PATHFINDEROPEN-01**



## QUADRATURE

Scalable multi-chip architectures enabled by cryogenic  
wireless/quantum-coherent network-in-package <sup>†</sup>

### D2.1: Specification Document

Contractual Date of Delivery	29/02/2024
Actual Date of Delivery	29/02/2024
Deliverable Dissemination Level	Confidential
Editor	F. Sebastiano (TU Delft), M. Babaie (TU Delft)
Contributors	TU Delft (leader), EPFL, UPC
Quality Assurance	E.Blokhina (EQUAL 1), A. Garcia (BSC)

---

<sup>†</sup>This project is supported by the European Commission under the Horizon Europe Framework Programme with Grant agreement no: 101099697.

## Document Revisions & Quality Assurance

Deliverable Number	D2.1
Deliverable Responsible	TU Delft
Work Package	WP2
Main Editor	F. Sebastiano (TU Delft), M. Babaie (TU Delft)

### Internal Reviewers

1. Elena Blokhina (EQUAL 1)
2. Artur Garcia (BSC)

### Revisions

Version	Date	By	Overview
1.0.0	19/2/2024	<i>Editor</i>	First draft.
1.1.0	28/2/2024	<i>Editor</i>	Reviewer changed.

### Legal Disclaimer

The information in this document is provided “as is”, and no guarantee or warranty is given that the information is fit for any particular purpose. The above referenced consortium members shall have no liability to third parties for damages of any kind including without limitation direct, special, indirect, or consequential damages that may result from the use of these materials subject to any liability which is mandatory due to applicable law. ©2023 by QUADRATURE Consortium.

# Executive Summary

The vision of the QUADRATURE project is to enable the scalability of quantum computers by adopting a multi-core architecture, in which multiple (relatively) small quantum processors are combined together to yield a larger computing power. Realizing this vision requires, among the several technologies and components to be developed, to demonstrate a wireless communication link (for classical non-quantum data) between different quantum cores. Towards this goal, the first step has been to analyze the system requirements and map them into the specifications for the wireless transceiver, which will be used in the follow-up phase as a guideline to design and prototype the integrated circuits implementing those functionalities. This report describes the wireless link specifications resulting from this process and their rationale.

The number of entangling operations between the cores has been analyzed by simulating the running of several benchmark quantum algorithms. Combining this information with a limit on the latency of the data exchange due to the limited qubit coherence, the data rate of the classical wireless link has been estimated, concluding that a 12-Gbps data rate would be sufficient to support an 8-core processor while ensuring 99.9% fidelity, in the worst case. Larger computers and higher fidelity can be supported in the future by augmenting the frequency and spatial diversity and by fine-tuning the quantum-traffic estimation. The transmission frequency for the wireless link is chosen to be 28 GHz by considering the effect of undesired emission of the classical transmitter on the fidelity of the quantum link, the power efficiency of the power amplifiers, the transceiver power consumption, the antenna size, and practical limitations of the available measurement setups. Based on those design choices for the data rate and the transmission frequency together with the developed electromagnetic model of the wireless channel, the link-budget optimization led to the following high-level specifications for the transceiver: a signal bandwidth of 2 GHz with 64-QAM modulation scheme, a transmitting output power of -1 dBm and a receiver noise figure of 5 dB. The feasibility of those specifications has been verified by mapping them on the practical design of both the transmitter and receiver, which resulted in a power estimation compatible with the 100-mW power budget set by the system requirements. In addition to deriving the specifications, advanced techniques are proposed for augmenting the performance of the wireless link by exploiting the reverberant static characteristic of the wireless channel with the time-reversal technique.

The results presented in this report can be used as the basis for the implementation of the cryogenic integrated-circuit prototype(s) of the wireless transceiver, thus allowing the project partners in the QUADRATURE's Work Package 2 (WP2) to start the transceiver's circuit design without any delay.

# Abbreviations and Acronyms

**NoC** Network-on-Chip

**QC** Quantum Computing

**BW** bandwidth

**QAM** quadrature amplitude modulation

**NF** Noise figure

**SNR** Signal-to-noise ratio

**TX** Transmitter

**RX** Receiver

**AWGN** Additive white Gaussian noise

$T_{noise}$  Noise temperature

$T_{ref}$  Reference temperature

**RT** Room temperature

**BER** Bit error rate

**EVM** error vector magnitude

**FSPL** Free space path loss

**PAPR** Peak to average power ratio

**OFDM** orthogonal frequency division multiplexing

**RMS** Root mean square

**LO** Local oscillator

**LOFT** LO feedthrough

**DAC** Digital-to-analog converter

**PA** Power amplifier

**QN** Quantization noise

**PN** Phase noise

$\omega_0$  Qubit Larmor frequency

$\omega_c$  Carrier frequency of Qubit Control Pulse

$\omega_R$  Qubit Rabi frequency

$B_0$  Static Magnetic Field

$F'$  Infidelities of qubit operation

$\theta$  Rotation angle of qubit operation

**ENBW** Equivalent Noise Band Width

$IQ_{mis}$  I/Q mismatch

**GDV** Group delay variation

**DC** Direct Current

**RF** Radio frequency

**AM** amplitude Modulation

**PM** Phase modulation

**PBO** Power back-off

**OP1dB** Output 1dB compression point

**ADC** Analog-to-digital converter

**SQNR** Signal-to-quantization-noise ratio

**PSD** Power spectral density

**LNA** Low noise amplifier

**SiGe BiCMOS** Silicon Germanium Bipolar Complementary Metal-Oxide-Semiconductor

**HBT** Heterojunction Bipolar Transistor

**FETs** Field-effect transistors

**CT** Cryogenic temperature

$J_c$  Collector Current Density

**TDC** Time-to-Digital Converter

**LPF** Low-pass Filter

**VCO** Voltage Controlled-Oscillator

**SFDR** Spurious Free Dynamic Range

**HQA** Hungarian Qubit Assignment

**QFT** Quantum Fourier Transform

**Mbps** Mega Bits per Second

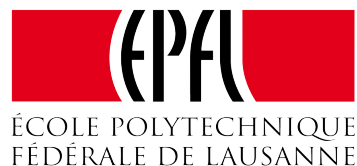
**Gbps** Giga Bits per Second

**QVol** Quantum Volume

**MAC** Media Access Control

## The QUADRATURE consortium is composed by

UPV	Coordinator	Spain
UPC	Beneficiary	Spain
TU Delft	Beneficiary	Netherlands
UoS	Beneficiary	Germany
UNICT	Beneficiary	Italy
EQUAL1	Beneficiary	Ireland
BSC CNS	Beneficiary	Spain
NUID UCD	Beneficiary	Ireland
EPFL	Associated partner	Switzerland



# Contents

<b>1</b>	<b>Introduction</b>	<b>13</b>
1.1	Organization of the report . . . . .	14
<b>2</b>	<b>Data rate analysis</b>	<b>16</b>
2.1	Traffic Analysis . . . . .	16
2.1.1	Packet Size . . . . .	16
2.1.2	Methodology . . . . .	17
2.1.3	Results . . . . .	17
2.2	Specifications on the data rate . . . . .	19
<b>3</b>	<b>RF Frequency Selection</b>	<b>22</b>
3.1	Interference with Qubits . . . . .	22
3.1.1	Background . . . . .	22
3.1.2	Theoretical Modeling . . . . .	26
3.1.3	Specification Calculation . . . . .	27
3.1.4	Conclusion . . . . .	29
3.2	Frequency specification . . . . .	29
<b>4</b>	<b>Channel model</b>	<b>31</b>
4.1	Wireless channel in a computer chip . . . . .	31
4.2	Quantum package design . . . . .	33
4.3	Conclusions . . . . .	35
<b>5</b>	<b>Link Budget</b>	<b>36</b>
5.1	Free Space Path Loss . . . . .	36
5.2	Selection of Modulation . . . . .	37
5.3	Sensitivity Calculations . . . . .	39
5.4	Output Power and EVM <sub>TX</sub> . . . . .	39
5.5	Conclusion . . . . .	41
<b>6</b>	<b>Mapping the specifications on the transmitter design</b>	<b>42</b>
6.1	I/Q Mismatch and LO Feedthrough . . . . .	43
6.2	Power Amplifier Non-linearity . . . . .	47
6.3	Group Delay Variation . . . . .	53
6.4	Other factors deteriorating EVM . . . . .	58
6.5	Power Consumption . . . . .	58
6.6	Spectrum Mask . . . . .	59
6.7	The resolution of DAC . . . . .	59
6.8	Conclusion . . . . .	60

<b>7 Mapping the specifications on the receiver design</b>	<b>62</b>
7.1 Introduction . . . . .	62
7.2 Overview of cryogenic LNA . . . . .	62
7.3 Improvement for LNA . . . . .	62
7.4 Noise and power trade-off for LNA . . . . .	65
7.5 Overview of cryogenic receiver . . . . .	67
7.6 Improvement for receiver . . . . .	67
7.7 Feasibility . . . . .	69
7.8 Conclusion . . . . .	69
<b>8 Advanced Transceiver Functionalities</b>	<b>71</b>
8.1 Overview of Time-Reversal . . . . .	71
8.2 Further Research Direction . . . . .	72
<b>9 Conclusions</b>	<b>73</b>

# List of Figures

1.1	The vision of QUADRATURE: many quantum-processor cores connected by both classical wireless channels and quantum entangling channels to enable scalability of the quantum computer. . . . .	14
2.1	Teleportation Circuit . . . . .	16
2.2	MAX non-local communications per timeslice for different core connectivities. . . . .	18
2.3	Results for packet size = $\lceil \log_2(\# \text{Cores}) \rceil + 2$ . . . . .	19
2.4	Results for packet size = $\lceil \log_2(\# \text{Qubits}) \rceil + 2$ . . . . .	20
3.1	A system-level view of RF channel and interference with qubits. . . . .	23
3.2	Control Signal and Bloch Sphere . . . . .	23
3.3	Amplitude Response v.s. $\omega$ [rad/s] of qubit filter for amplitude noise for different rotation angles with $\omega_0 = 2 \cdot \pi \cdot 12\text{GHz}$ and $\omega_R = 2 \cdot \pi \cdot 10\text{MHz}$ . . . . .	24
3.4	Amplitude Response v.s. $\alpha$ of qubit filter for amplitude noise for different rotation angles. . . . .	25
3.5	Amplitude Response v.s. $\omega$ [rad/s] of qubit filter in idle for amplitude noise for different idle duration time . . . . .	26
3.6	$T_{idle}$ vs $S_{Tx}(\omega)$ with $F' = 1 \times 10^{-6}$ . . . . .	28
3.7	Reference of Transmitter Spectrum Mask . . . . .	28
3.8	Efficiency of state-of-the-art CMOS power amplifiers at their 1-dB power compression points versus their operating frequencies. . . . .	30
4.1	Schematic of the layers of a flip-chip package [3]. . . . .	31
4.2	Channel behavior and characterization for room and cryogenic temperatures . . . . .	33
4.3	Proposal of the quantum cavity . . . . .	33
4.4	Quantum Package in CST . . . . .	34
4.5	Isolation of the QChip . . . . .	34
4.6	Isolation of the QChip . . . . .	35
5.1	Free space path loss at 28 GHz . . . . .	37
5.2	BER vs. SNR . . . . .	38
5.3	BER vs. SNR . . . . .	40
6.1	Conventional I/Q transmitter block diagram . . . . .	42
6.2	Constellation Diagram . . . . .	43
6.3	Conventional I/Q transmitter block diagram and . . . . .	44
6.4	I/Q mismatch in direct-conversion transmitter . . . . .	45
6.5	Image and LO feedthrough in direct-conversion transmitter . . . . .	45

6.6 Impact of I/Q mismatch in constellation diagram . . . . .	45
6.7 The relation between I/Q mismatch and EVM(dB) . . . . .	46
6.8 Impact of LO feedthrough in constellation diagram . . . . .	46
6.9 PA AM/AM Distortion . . . . .	47
6.10 . . . . .	48
6.11 Common source stage with parasitic capacitance . . . . .	49
6.12 . . . . .	49
6.13 The relationship between input voltage and phase of output . . . . .	50
6.14 . . . . .	51
6.15 . . . . .	51
6.16 The relationship between OP1dB and EVM when using a 64QAM signal with an output power of -1dBm. . . . .	52
6.17 Phase shift in transmitter . . . . .	53
6.18 Impact of non-linear phase shift in the frequency domain. . . . .	54
6.19 Impact of non-linear phase shift in the time domain. . . . .	54
6.20 . . . . .	54
6.21 The simplest group delay variation model. . . . .	55
6.22 Simulation of group delay variation in the time domain. . . . .	56
6.23 The constellation diagram of 4-QAM signal. . . . .	57
6.24 . . . . .	57
6.25 The PSD of a transmitted signal. . . . .	60
7.1 Topology of the BiCMOS wideband low-noise amplifier . . . . .	63
7.2 Measured noise temperature of the LNA . . . . .	63
7.3 Anticipated statics of the current variation versus the supply voltage using the cryogenic static models. . . . .	64
7.4 Base resistance $r_b$ as a function of collector current densities . . . . .	66
7.5 Minimum noise temperature $T_{min}$ as a function of collector current densities . . . . .	66
7.6 Minimum noise temperature ( $T_{min}$ ) as a function of both the frequency for four different current densities: (a) $J_c = 0.01 \text{ mA}/\mu\text{m}^2$ , (b) $J_c = 0.1 \text{ mA}/\mu\text{m}^2$ , (c) $J_c = 1 \text{ mA}/\mu\text{m}^2$ , and (d) $J_c = 20 \text{ mA}/\mu\text{m}^2$ . . . . .	67
7.7 Architecture of the lockin receiver . . . . .	68
7.8 Micrograph of the lockin receiver, Tech: SiGe BiCMOS IHP 130nm, 1.4 V, Date: Tapeout on 15th Dec. 2023, will be measured in Jun. 2024 . . . . .	68
7.9 Architecture of improved polar receiver . . . . .	69
8.1 Time reversal in a wireless in-package environment [7] . . . . .	72

# List of Tables

2.1	Bandwidth needed (Mbps) for different circuits, number of cores (8, 12, and 16), and desired coherence for the line (most restrictive) topology.	20
3.1	Infidelity of the qubit in operation and idle	27
3.2	PSD Calculation Parameters and Requirement	29
4.1	Characteristics of the layers in a flip-chip package and default dimensions. $\epsilon_r$ is the relative permittivity of the material, $\tan(\delta)$ is the loss tangent, and $\rho$ refers to the conductivity. PEC stands for perfect electrical conductor (lossless material of infinite conductivity) [36].	32
5.1	System Requirements	36
5.2	Link budget	41
6.1	EVM Requirements	60
6.2	Transmitter Design Specifications	61
7.1	Specifications of the existing LNA	64
7.2	Power Consumption Distribution	70
7.3	Receiver Performance Specifications	70

# 1. Introduction

The vision of the QUADRATURE project is to enable the scalability of quantum computers by adopting a multi-core architecture, in which multiple (relatively) small quantum processors are combined together to yield a larger computing power [4]. Realizing this vision requires the implementation of a number of different components, as shown in Fig. 1.1, and the development of several innovative technologies, such as multi-core compilation of quantum algorithms, inter-core quantum communication, and classical-data inter-core communication.

This report focuses on the classical-data inter-core communication. During the execution of the quantum algorithm, it should be possible to entangle qubits from different cores<sup>1</sup>. Typical entangling protocols require the exchange of both classical and quantum information among the cores. Similar to the current trends in Network-on-Chip research, a wireless communication channel has been proposed in QUADRATURE for its flexibility [4]. This report describes the requirements that such wireless communication should satisfy to support the needs of the system and maps such requirements on the specifications for the receiver and the transmitter. Those specifications will then be used as the basis for the implementation of the integrated-circuit prototype(s) of the wireless transceiver. Unlike standard wireless transceiver, the QUADRATURE transceiver will operate at cryogenic temperature (at 4 K) due to the need of operating in close proximity to the cryogenic qubits, and will operate in the enclosed and static environment of a cryogenic chamber. Those aspects both introduces significant challenges, such as the limited power consumption (< 100 mW/transceiver), and allow for innovative design choices, e.g., a possible static calibration of the wireless-channel response.

As the system requirements span over the whole project and over multiple Work Packages (WP), several partners contributed directly or indirectly to the system analysis and the drafting of the system requirements. In particular, the partners in WP3, mainly UPC, performed an analysis of the traffic between the cores and simulated the electromagnetic response of the wireless channel, with input from UoS and EQUAL1 on the physical geometry of the proposed quantum computer. Within WP2, TUD analysed those requirements to derive the specifications for the transceiver and mapped them, in collaboration with EPFL, on possible implementation of the transmitter and receiver circuits, which will be implemented in the future by TUD and EPFL.

It is important to point out that, at such an early stage of the project, the system requirements are based on a number of assumptions that will necessarily need to be adapted along the progress made across the different research directions within the project, e.g., advances in the compilation strategies and more accurate simulation

---

<sup>1</sup>This is necessary to ensure that the computational power of the whole quantum computer scales exponentially with the number of qubits, as necessary to achieve the so-called *quantum speed-up* or *quantum advantage*, instead of just proportionally with the number of cores.

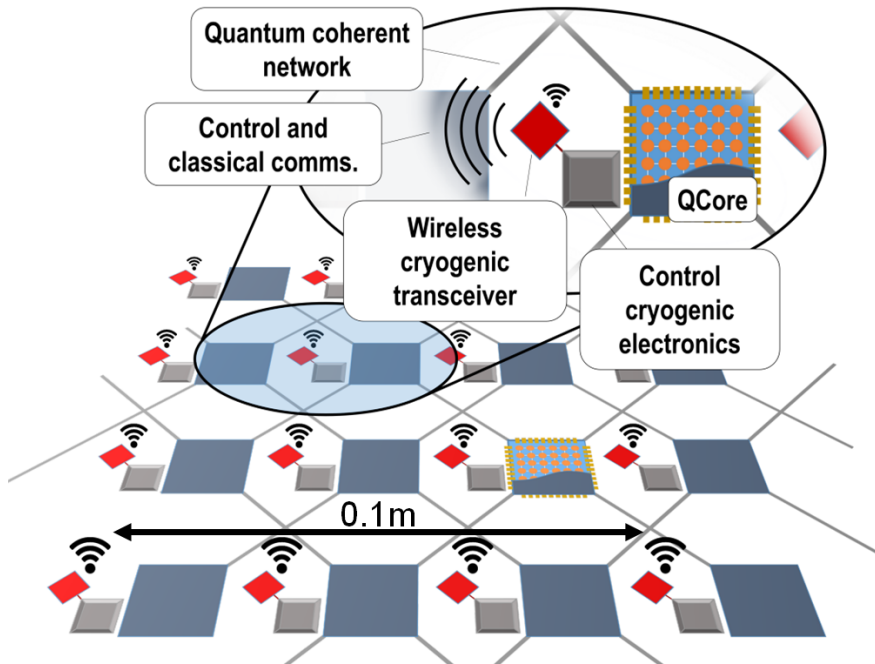


Figure 1.1: The vision of QUADRATURE: many quantum-processor cores connected by both classical wireless channels and quantum entangling channels to enable scalability of the quantum computer.

tools will refine the traffic profiling and alter the requirement on the wireless channel data rate, or changes in the system geometry induced by the quantum-communication medium may affect the channel response. Still, deriving a complete set of specifications is a crucial starting point for enabling the relevant part of the consortium (TUD + EPFL) to start the experimental validation of the wireless infrastructure. In the following chapters, several assumptions have been made based on the current understanding of the system and the state of the art. A few design choices are also made as a balance between what can be implemented right now (based on the current state of the art) and the push to go beyond the state of the art to explore fundamental limitations that could limit the system performance.

## 1.1 Organization of the report

As a first step, running a few benchmark quantum algorithms is simulated on a few prototype architectures of the multi-core quantum computer. By analysing the number of entangling operations between cores, the amount of data to be exchanged is simulated, and by posing a limit on the latency of the data exchange due to the limited qubit coherence, the data rate of the wireless communication is derived in Chapter 2.

Chapter 3 analyses the different trade-offs for choosing the RF frequency of the wireless channels, such as the size of the transmitting and receiving antennas, the minimization of interference on the qubit operation, the power dissipation in the transceiver electronics, and practical limitations in the experimental validations.

Chapter 4 presents a physical electromagnetic model of the wireless channel, used to identify specific features that affect the link budget analysed in Chapter 5 and the

design of the transmitter and the receiver, whose implementation feasibility is studied in Chapter 6 and 7, respectively.

Finally, Chapter 8 presents a proposal for advanced functionalities of the transceiver that could exploit the specificity of the proposed system to alleviate some of the implementation challenges and result in higher performance. The conclusions are drawn and summarized in Chapter 9.

## 2. Data rate analysis

### 2.1 Traffic Analysis

In this Section, we estimate the bandwidth needed for the wireless channel within the scope of QUADRATURE's architectural proposal. Throughout the execution of a quantum circuit in a modular architecture, qubits need to be moved across cores, making sure every time two qubits interact, they are placed within the same core. It is the compiler's task to minimize the number of quantum state transfers along the execution of the circuit.

We assume the case where quantum states are transferred across modules using the teleportation [14] protocol (see Figure 2.1). The task for the wireless channel is to communicate the measurement bits to correct the possible bit- or phase-flip in the destination qubit ( $|\Phi^+\rangle_B$  in Figure 2.1).

#### 2.1.1 Packet Size

In order to perform a teleportation, we need to transfer the two measured bits in the circuit (associated with bit- and phase-flips) and an identifier of the destination qubit, to which these corrections should be applied. Therefore, the packet size to transmit for each inter-core quantum state transfer is as follows:

$$\text{packet size} = \text{destination}_{id} + 2$$

Remains to define the size of the  $\text{destination}_{id}$ . Since it is still unclear how cores will be connected among them, we analyze two scenarios:

- **1 communication qubit per core:** in this scenario, each core has a single physical qubit devoted to communication. This qubit will always hold one part of the entangled state. Therefore, in order to identify which operations we need to perform for the quantum teleportation to be successful, we only need to know in which core the corrections will happen (the destination core of the teleportation).

$$\text{destination}_{id} = \lceil \log_2(\#\text{Cores}) \rceil$$

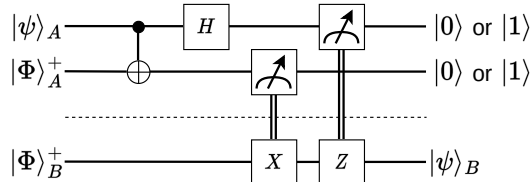


Figure 2.1: Teleportation Circuit

- **Enabling all qubits for communication:** in this other scenario, each physical qubit can be used to perform teleportation. Each qubit in the processor (regardless of the core where the qubit is located) has an identifier, ranging from 0 to #Qubits.

$$\text{destination}_id = \lceil \log_2(\# \text{Qubits}) \rceil$$

### 2.1.2 Methodology

To estimate the required bandwidth, we compile, using the Hungarian Qubit Assignment (HQA) algorithm [11], four different quantum algorithms onto a modular architecture with different topologies. We fix the number of qubits per core to 64 and increase the number of cores in the architecture up to 16 (for a total of 1024 qubits).

The selected circuits represent a diverse set of quantum algorithms. We compile two unstructured algorithms (Random Circuit and Quantum Volume Circuit) and two structured instances (Quantum Fourier Transform and Cuccaro Adder). The algorithms have been obtained from the Qiskit circuit library.

For the compilation, we first split each circuit into timeslices, the set of gates that can be executed simultaneously. HQA obtains, for each timeslice, an assignment of qubits to cores, aiming to minimize the number of quantum state transfers between timeslices.

Three different core connectivities have been tested. *All-to-All*, where all cores are connected to one another (graph diameter = 1), *Line*, where cores are connected in a 1D array structure (graph diameter = number of cores), and *Ring*, where cores are connected in a circular way (graph diameter = number of cores / 2).

The number of classical bits we need to transfer over the wireless channel depends on the number of non-local communications and the desired packet size.

Once the number of bits to transfer is set, the time devoted to using the wireless channel remains to be defined. A lower communication time results in a higher bandwidth.

Considering the qubit decoherence time, we define the necessary communication time within the qubit lifetime. Relying on the experimental results from [31], the decoherence time of electron spin qubits (without implementing the dynamic decoupling technique for extending the qubit lifetime) is  $T_2 = 268 \mu\text{s}$ . Assuming an exponential decay of the qubit coherence over time, the qubit coherent state after  $t \mu\text{s}$  can be obtained from  $e^{-t/T_2}$ .

In the results presented, the bandwidth was obtained compared to the coherence of the qubits after the communication time.

### 2.1.3 Results

The maximum number of teleportations required to execute the chosen circuits is depicted in Figure 2.2. This value is obtained by assigning qubits to cores for each timeslice and represents the highest number of teleportations necessary to fulfil two consecutive assignments.

Using the number of teleportations needed and packet size, we can estimate the bandwidth needed (inversely proportional to the communication time) and relate it to the decoherence induced by the idling time of the qubits waiting for the classical communication to happen.

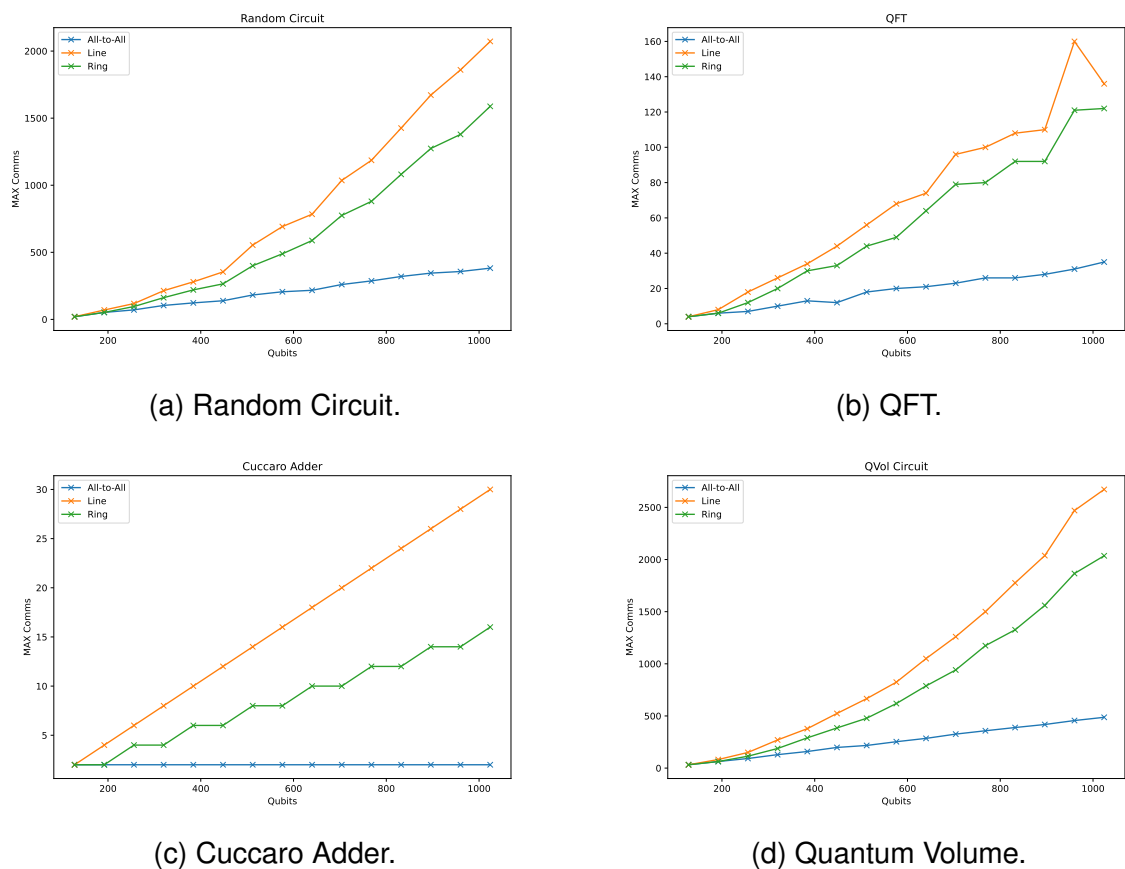
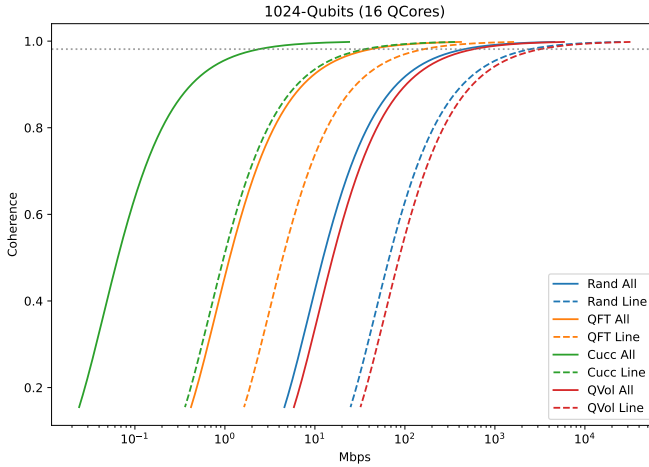
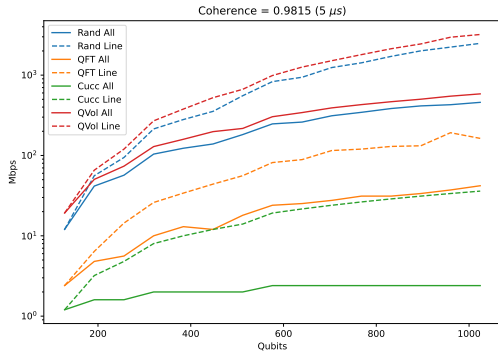
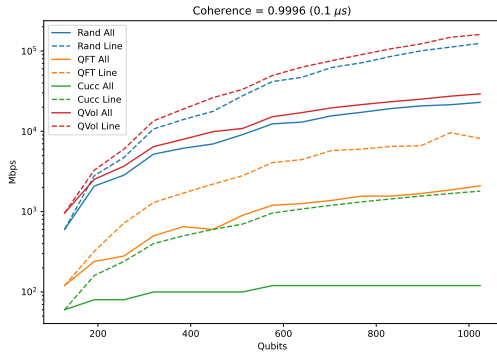


Figure 2.2: MAX non-local communications per timeslice for different core connectivities.



(a) Bandwidth and Coherence for a 1024-qubit system.

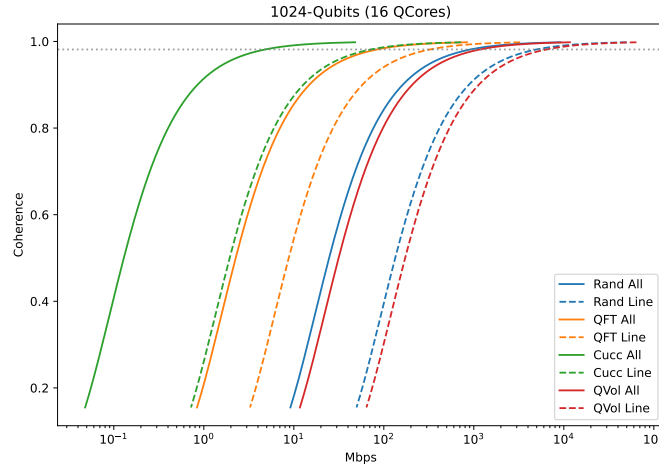
(b) Bandwidth and System Size for transmission time of  $5\mu s$ .(c) Bandwidth and System Size for transmission time of  $100ns$ .Figure 2.3: Results for packet size =  $\lceil \log_2(\#Cores) \rceil + 2$ 

Figures 2.3 and 2.4 depict the bandwidth needed for the different packet sizes. Figures 2.3a and 2.4a show the decoherence induced to the qubit for different bandwidths (the lower the bandwidth is, the higher the idling time is, and thus the decoherence of the qubit increases). Figures 2.3b, 2.4b and 2.3c, 2.4c show the bandwidth needed for a fixed coherence when increasing the system size, meaning the number of cores increases by one, incrementing the total number of qubits by 64 (number of qubits per core is fixed to 64).

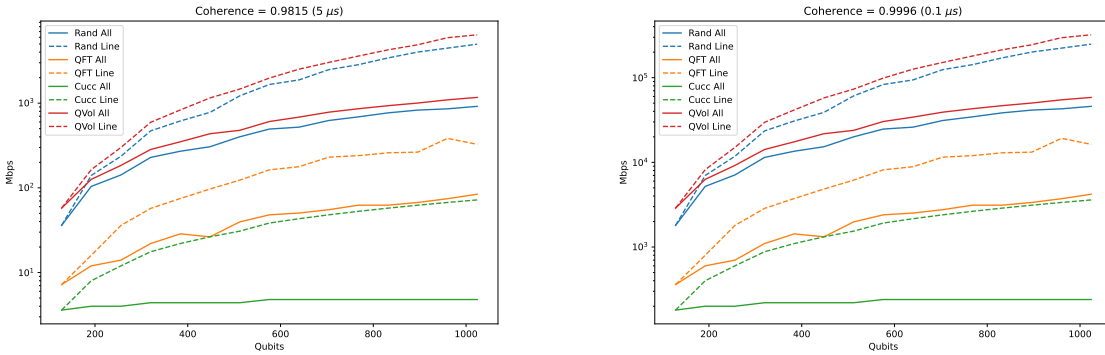
Table 2.1 shows, for the smaller packet size, the needed Mbps for some fixed coherence.

## 2.2 Specifications on the data rate

The data rate requirements in Table 2.1 cover a wide range from just 2 Mbps up to almost 600 Gbps, with a strong dependence on the type of algorithm, the achieved qubit fidelity, and the number of cores. While it is clear that a higher data rate can support a larger system or a system with higher performance, e.g., higher fidelity, there are stringent limitations on the power consumption of the transceiver due to the limited cooling



(a) Bandwidth and Coherence for a 1024-qubit system.

Figure 2.4: Results for packet size =  $\lceil \log_2(\#Qubits) \rceil + 2$ 

Coherence	Random		QFT		Cuccaro		QVol	
	8	16	8	16	8	16	8	16
0.9999	103.353	463.857	10.447	30.446	2.611	6.716	124.247	598.179
0.999	10.330	46.364	1.044	3.043	261	671	12.419	59.790
0.99	1.028	4.615	103	302	25	66	1.236	5.952
0.9	98	440	9	28	2	6	117	567

Table 2.1: Bandwidth needed (Mbps) for different circuits, number of cores (8, 12, and 16), and desired coherence for the line (most restrictive) topology.

budget of existing cryogenic refrigerators. Considering a total power budget below 100 mW for the whole transceiver, the data rate should not significantly exceed the requirements of the 5G standard [1], for which such power budget and practical integrated implementation are deemed realistic. As a consequence, we choose to limit the data rate to **12 Gbps**. As shown in Table 2.1, such data rate would directly support an **8-core processor with 99.9% fidelity**, which would represent a very significant milestone for quantum computing. In addition, such a baseline scenario assume a single wireless channel at a single frequency shared in time multiplexing by all the transceivers in each core. Once such a point-to-point communication is demonstrated, frequency multiplexing could be relatively easily added by using more channels in the spectrum, noticing, as it will be explained in Chapter 3, that a large amount of the spectrum is available since no wireless standard or regulation must be enforced. Furthermore, as proposed in Chapter 8, the system may be augmented with spatial diversity by adopting advanced transceiver functionalities. Spatial and frequency diversity together could realistically increase the data rate by  $50\times$ , bringing the point-to-point physical data rate of 12 Gbps to the effective 600 Gbps required by the most stringent scenario. Also, the higher available data rate can be employed to account for any overhead introduced by the MAC layer, which has been ignored in the present estimation.

Finally, it must be highlighted that the worst scenario, i.e., the scenarios requiring the highest data rate, comprises benchmark algorithms (quantum volume, random circuit) that are specifically designed to stress the system performance, but do not necessarily have a practical use. The other algorithms with practical applications (Cuccaro, QFT) are much more structured, resulting in a  $20\times$  more relaxed requirement on the data rate. Thus, additional work on the traffic analysis could also relax the data rate requirements. Also, any future improvement of the qubit coherence time will proportionally relax the requirement on the communication latency and, hence, on the data rate.

## 3. RF Frequency Selection

### 3.1 Interference with Qubits

In this part, the impact of classical channels on the qubit will be analyzed in detail. The aim is to provide a reference for the spectral mask design of the transmitter with a negligible impact on qubits. This section is organized as follows: Sec.3.1.1 describes the interference from the RF communication channel on the qubits, which is followed by background information and how to map such interference on qubit operations. In Sec.3.1.2, a theoretical model is presented used for the following calculation and analysis. This is followed by the Power Spectrum Density (PSD) and power of spurious tone calculation of the transmitter. Finally, the conclusion is drawn in Sec. 3.1.4.

#### 3.1.1 Background

An overview of interference with qubits is shown in Fig.3.1, which illustrates the undesired impact of RF communication channel on qubits. The physical platform shown here is based on the single-electron spin qubits, which is currently the technology used in QUADRATURE.

For spin qubits, an external static magnetic field  $B_0$  shown in Fig.3.1 is applied to resonate with the Larmor frequency of each qubit  $\omega_0(\propto B_0)$ . The range of  $\omega_0$  is between  $10GHz$  to  $16GHz$  [33]. For single-qubit operation, a varying magnetic field  $B(t)$  oscillating at the Larmor frequency is required. To generate this field, a varying current or voltage in the driveline is required shown in Fig. 3.1. In the case of an oscillating voltage, the required microwave is generated by modulating a carrier with an envelope. The frequency of the carrier should be resonant with Larmor frequency i.e.  $\omega_c = \omega_0$ , and the envelope  $|V|$  is proportional to Rabi frequency of qubit i.e.  $|V| \propto \omega_R$ .

Operating on a single qubit is equivalent to performing a rotation of the qubit state in the Bloch sphere, as shown in 3.2. The rotation angle of operation ( $\theta = \omega_R \cdot T$ ) is determined both by the amplitude ( $|V|$ ) and duration ( $T$ ) of the microwave wave pulse.

To evaluate the accuracy of an actual qubit operation, the fidelity ( $F$ ) is introduced, which is 100 % in the case is perfect. In practice, infidelities( $F' = 1 - F$ ) ranging from  $10^{-2}$  to  $10^{-4}$  is more typical [8] required for fault-tolerant quantum computation. Infidelities are mainly limited by the non-idealities in the driving signal and physical implementation of the qubit itself. In our project, if the interference from the RF channel coupled with the driveline, it could be shown as an amplitude noise signal ( $\delta\omega_R(t)$ ) on the driveline.  $\delta\omega_R(t)$  can be regarded as white noise with power spectral densities  $S_R(\omega)$ .

According to the status of the qubit operations, it can be divided into two cases: qubit in operation and qubit in idle. The qubit fidelities models are discussed as follows.

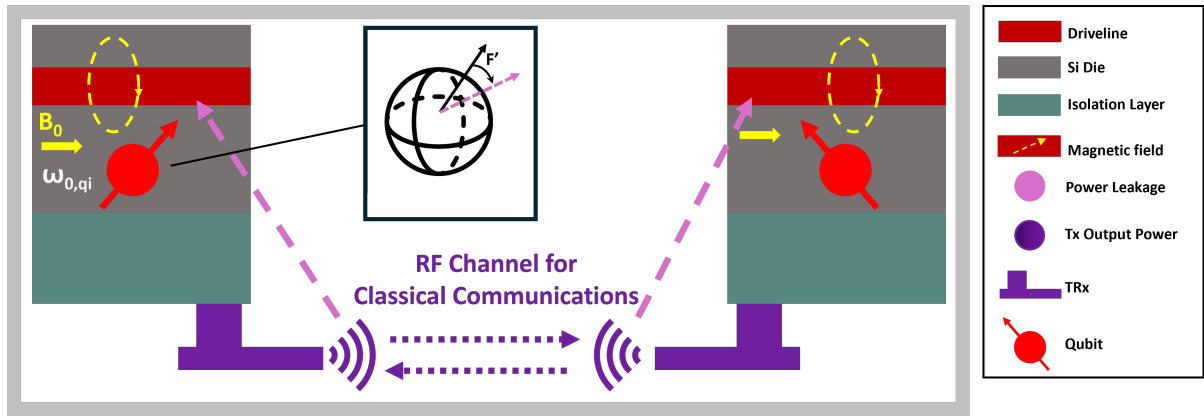


Figure 3.1: A system-level view of RF channel and interference with qubits. The purple chain indicates classical communication among different transceivers, and the light purple chain means the power leakage from the classical channel to the qubits shown in red. Such leakage could be coupled on the driveline of qubits, which will degrade the state of the qubit. Finally, this interference will contribute to the infidelity ( $F'$ ) of quantum operations illustrated in the Bloch sphere. Furthermore, each qubit has a unique Larmor frequency ( $\omega_{0,qi}$ ).

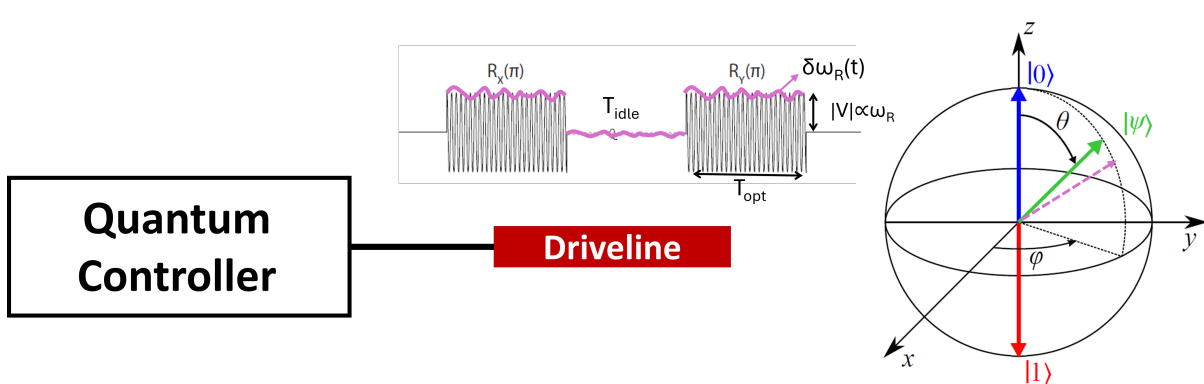


Figure 3.2: Control Signal and Bloch Sphere

When a qubit is in operation, such interference can be modeled as fluctuations in the envelope of the control signal, which means  $\omega_R(t) = \omega_R + \delta\omega_R(t)$ . The method presented in Ref. [16] can be adopted to compute the infidelity as a function of the noise spectrum. The infidelity model from Ref. [39] is shown in Eq.3.1

$$F'_{opt} = \frac{1}{\pi} \int_{\omega_{min}}^{\infty} \frac{S_R(\omega)}{\omega_R^2} |H_R(\omega)|^2 d\omega \quad (3.1)$$

where,  $|H(\omega)|^2$  is the intrinsic qubit filter function, indicating that for different frequencies, qubit has a different sensitivity.  $|H_R(\omega)|^2$  can be expressed as:

$$|H_R(\omega)|^2 = \frac{\sin^2(\alpha \cdot \frac{\theta}{2})}{\alpha^2} \quad (3.2)$$

where  $\alpha = \frac{\omega - \omega_0}{\omega_R}$  is the frequency normalized to the Rabi frequency.

The amplitude response of the Qubit filter for amplitude noise with frequency and normalized coefficient  $\alpha$  are shown in Fig.3.3 and Fig/3.4. As shown, these responses have a Band-Pass-Filter(BPF) characteristics.

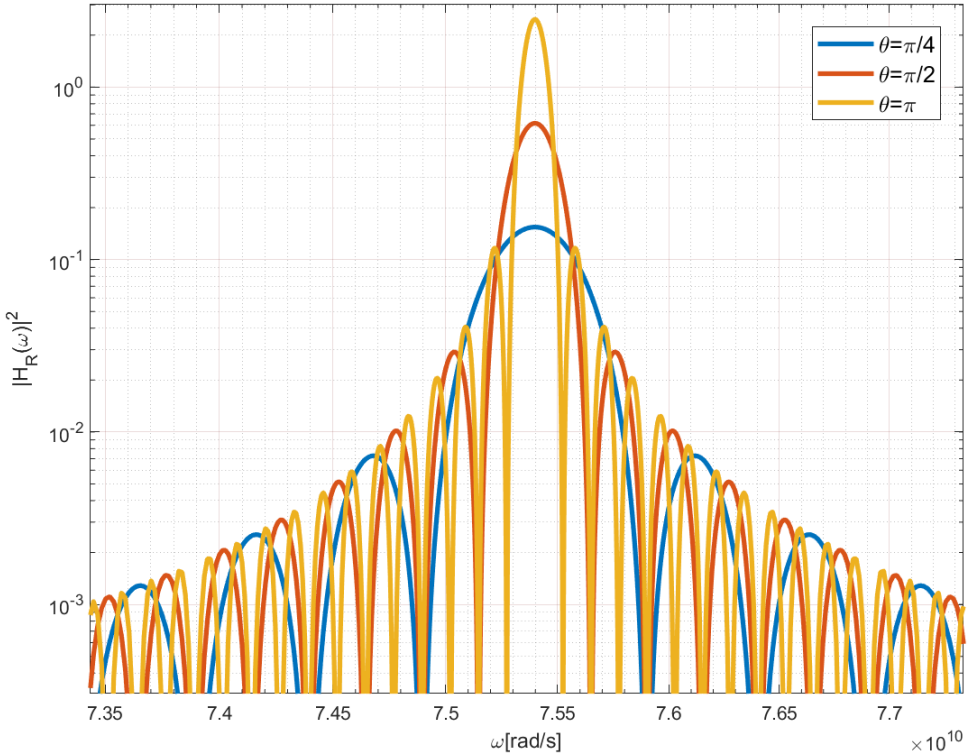


Figure 3.3: Amplitude Response v.s.  $\omega$ [rad/s] of qubit filter for amplitude noise for different rotation angles with  $\omega_0 = 2 \cdot \pi \cdot 12GHz$  and  $\omega_R = 2 \cdot \pi \cdot 10MHz$ .

Another case is qubit in idle. If we run a quantum algorithm, qubit can be idle for a while for quantum error correction or waiting for the operations on other qubits to finish. During the idle period, the interference could also be coupled on the driveline as a noise signal to degrade the state of the qubit. The infidelity of qubit in idle is shown as below:

$$F'_{idle} = \frac{1}{\pi} \int_0^{\infty} S_R(\omega) \cdot |H_n(\omega)|^2 \cdot d\omega \quad (3.3)$$

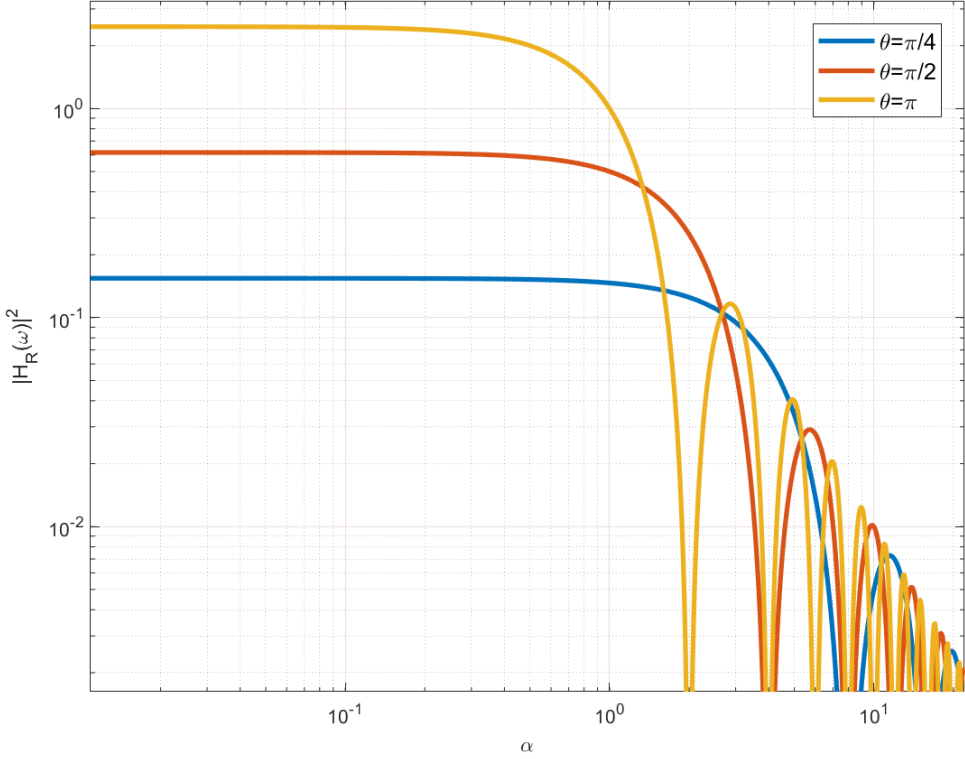


Figure 3.4: Amplitude Response v.s.  $\alpha$  of qubit filter for amplitude noise for different rotation angles.

Where,  $|H_n(\omega)|^2$  can be expressed as:

$$|H_n(\omega)|^2 = 2 \cdot \frac{\sin^2\left(\frac{T_{\text{idle}}}{2} \cdot (\omega - \omega_0)\right)}{(\omega - \omega_0)^2} \quad (3.4)$$

The duration of qubit in idle is  $T_{\text{idle}}$ . The amplitude response is shown in Fig. 3.5. Similarly, the response is also shown as a BPF characteristic.

Besides the noise, a spurious tone from the transmitter could also be directly coupled on top of qubit Larmor frequency. The presence of such a tone will also reduce the qubit fidelities [39]. The infidelity due to spurs is shown as follows:

$$F'_{\text{idle,spur}} = \frac{1}{4} \cdot \omega_{\text{spur}}^2 \cdot T_{\text{idle}}^2 \quad (3.5)$$

where  $\omega_{\text{spur}}$  is the contribution of this tone to the un-desired Rabi frequency.

Since the noise in the band of interest can be approximated as white noise, equivalent noise bandwidth(ENBW) can be introduced to simplify calculations. The results based on the Ref. [39] are summarised in the Tab. 3.1. The infidelity of single-qubit operation can be re-written as  $F' = \frac{1}{4} S_R(\omega) T_{\text{opt}}$ , where  $T_{\text{opt}} = |\theta|/\omega_R$  is the duration of the single-qubit operation. Considering the worst case, the minimum noise PSD requirement should be calculated to meet the high-fidelity qubit operations. Typically, the duration of qubit in idle ( $T_{\text{idle}} \sim 10\mu\text{s}$  is tens of qubit in operation(e.g.  $T_{\text{opt}} \sim 0.1\mu\text{s}$  for typical single-qubit  $X(\pi)$  gate)). Therefore, the noise PSD requirement of qubits in idle is much higher than the case in operation. To simplify the calculation, the infidelity of qubits in idle is used in the following modeling and calculation.

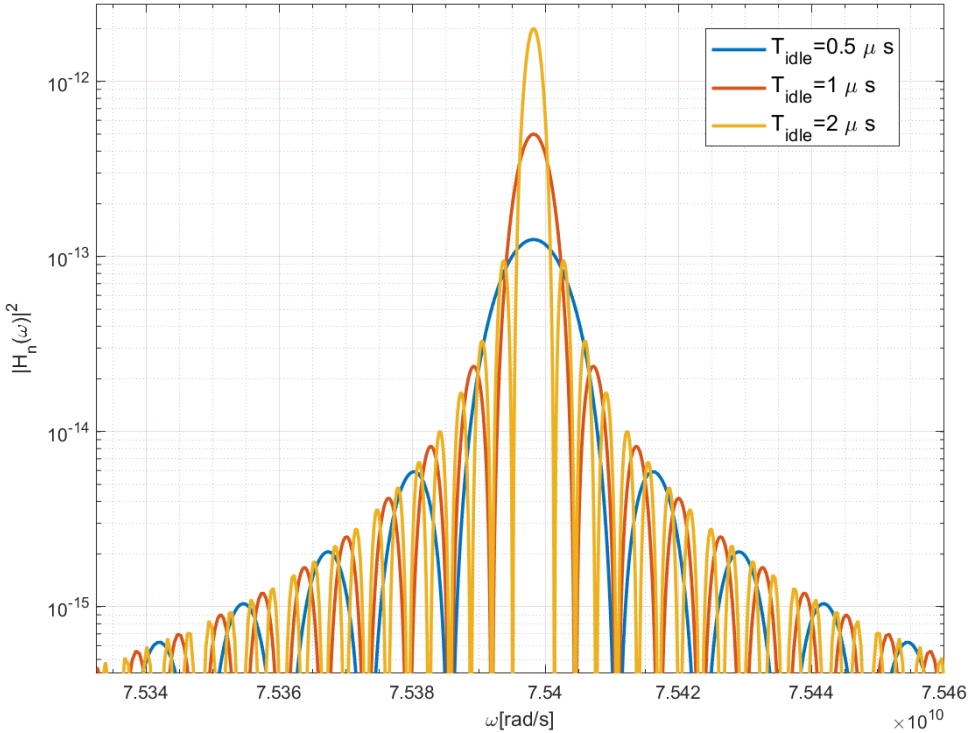


Figure 3.5: Amplitude Response v.s.  $\omega$  [rad/s] of qubit filter in idle for amplitude noise for different idle duration time

### 3.1.2 Theoretical Modeling

The transmit power spectral density(PSD) from the transmitter in a classical wireless channel is  $S_{Tx}(\omega)$ . Considering the isolation loss ( $L$ ) from the isolator, the energy leaked to qubit can be expressed as  $S_Q(\omega) = S_{Tx}(\omega)/L$ .

The energy can be converted to the voltage spectral density of the fluctuations ( $S_V(\omega)$ ) in the envelope for a qubit-driving microwave pulse.

$$S_V(\omega) = S_Q(\omega) \cdot R_0 \quad (3.6)$$

where  $R_0$  represents the impedance of a transmission line and suppose such line here is terminated with a matched resistor.

As discussed before, qubit fidelity is influenced by the fluctuations( $\delta\omega(t)$ ) in the rabi frequency  $\omega_R$ [Hz], which is proportional to the envelope amplitude of the microwave driving pulse  $V$ [V]. They can related by the translation factor  $k$ [Hz/V] =  $\frac{\omega_R}{|V|}$ .

Then, combining translation factor  $k$ , with the formula 3.7, we can get the spectral density  $S_R(\omega)$ [Hz]of the noise signal applied to the qubit.

$$S_R(\omega) = S_V(\omega) \cdot k^2 \quad (3.7)$$

According to the assumption in the previous section, qubit in idle, the more stringent situation, is discussed here. The infidelity of the qubit in idle is:

$$F' = S_R(\omega) \cdot T_{idle} \quad (3.8)$$

Combining eq. 3.6 to 3.8, the infidelity of the qubit due to the noise PSD from the classical wireless channel can be modeled as:

$Q_{status}$	$\text{ENBW} (= \int_0^\infty \left  \frac{H(\omega)}{H_{\max}} \right ^2 d\omega)$	$ H_{\max} ^2$	$\int_0^\infty  H(\omega) ^2 d\omega$	$F'$
Op.	$\omega_R \frac{\pi}{ \theta }$	$\frac{1}{4}\theta^2$	$\frac{1}{4}\omega_R \pi  \theta $	$\frac{1}{4}S_R(\omega) \frac{ \theta }{\omega_R}$
Idle(noise)	$\frac{2\pi}{T_{idle}}$	$T_{idle}^2/2$	$\pi T_{idle}$	$S_R(\omega) \cdot T_{idle}$
Idle(spur)				$\frac{1}{4} \cdot \omega_{\text{spur}}^2 \cdot T_{idle}^2$

Table 3.1: Infidelity of the qubit in operation and idle

In this table,  $Q_{status}$  presents the status of the qubit, either in *OP*.(single qubit operation) or in *Idle*(idle gate);  $\theta$  is the rotation angle on Bloch sphere; noise power spectral densities(PSD) by  $S_R(\omega)$ ; qubit intrinsic filter by  $|H(\omega)|^2$ ; ENBW by equivalent noise bandwidth;  $F'$  by infidelity.

$$F' = \frac{S_{Tx}(\omega) \cdot R_0 \cdot k^2 \cdot T_{idle}}{L} \quad (3.9)$$

Similarly, the infidelity of the qubit due to spur  $\delta_{\text{spur}}[\text{dBm}]$  from TX can also be modeled as:

$$F' = \frac{1}{4} \frac{\delta_{\text{spur}}}{L} \cdot R_0 \cdot k^2 \cdot T_{idle}^2 \quad (3.10)$$

### 3.1.3 Specification Calculation

With the model provided in Section 3.1.2, the transmitter PSD and spur calculation in the classical wireless channel can now be derived. Compared with the reported most stringent infidelity of  $F' = 1 \times 10^{-4}$  for fault-tolerant quantum computation, the infidelity caused by wireless communication should be sufficiently low to ensure qubit is in a safe region during the RF communication. We assume  $F' = 1 \times 10^{-6}$  to quantify such impact. Isolation loss ( $L = 20\text{dB}$ ) from the classical to quantum channel is assumed. Regarding the translation factor  $k (= \omega_R / |V|)$ , the values provided assume a qubit processor based on Voltage-Control driving way, where the amplitude( $|V|$ ) of  $2mV$  at the gate is required for a Rabi frequency( $\omega_R$ ) of  $1\text{MHz}$ (close to the value reported in [19]). Therefore, the translation factor  $k$  can be calculated as:

$$k = \frac{\omega_R}{|V|} = 5 \cdot 10^8 [\text{Hz}/V] \quad (3.11)$$

Typically, the idle time of qubit operation is  $10\mu\text{s}$ . In case of the reported maximum Lamour frequency ( $\omega_0 = 12\text{GHz}$ ) [33], the parameters mentioned above and final calculated PSD and spur are shown in the Tab. 3.2

Fig. 3.6 shows the relation between  $T_{idle}$  and PSD of the transmitter, which matches the theoretical analysis before. With a shorter idling time, the PSD requirement could be relieved.

To further reduce the effect of interference on the qubit, the larger possible bandwidth with the same PSD level is preferred in the design of the transmitter spectrum mask. Here, we choose  $20\text{MHz}$ (considering the maximum reported Rabi frequency  $10\text{MHz}$  [33]) as the bandwidth requirement for the spectrum mask.

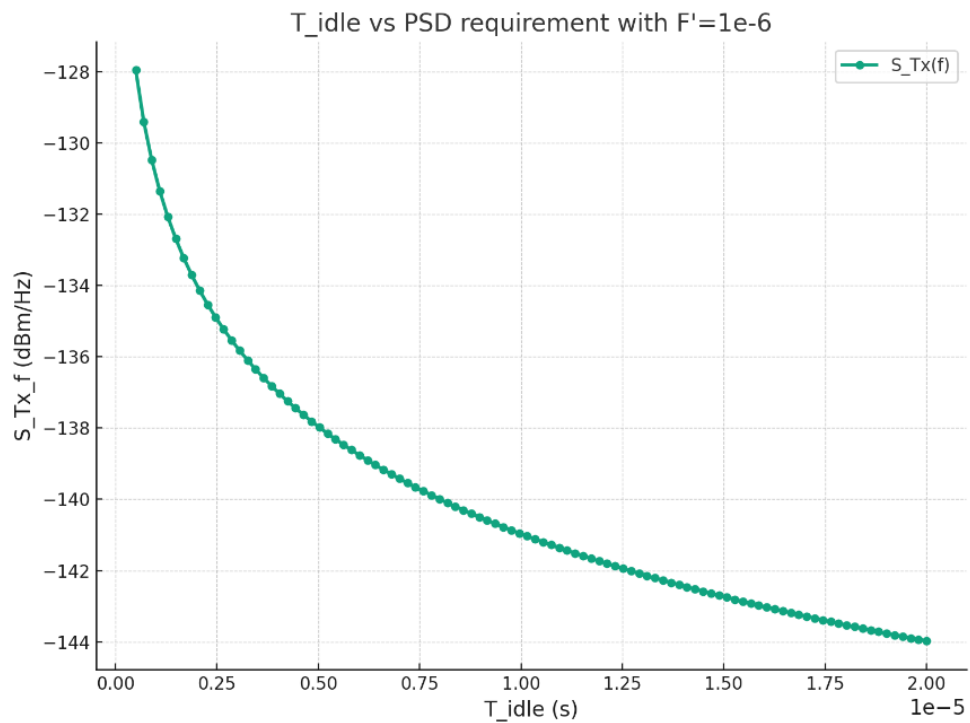


Figure 3.6:  $T_{idle}$  vs  $S_{Tx}(\omega)$  with  $F' = 1 \times 10^{-6}$

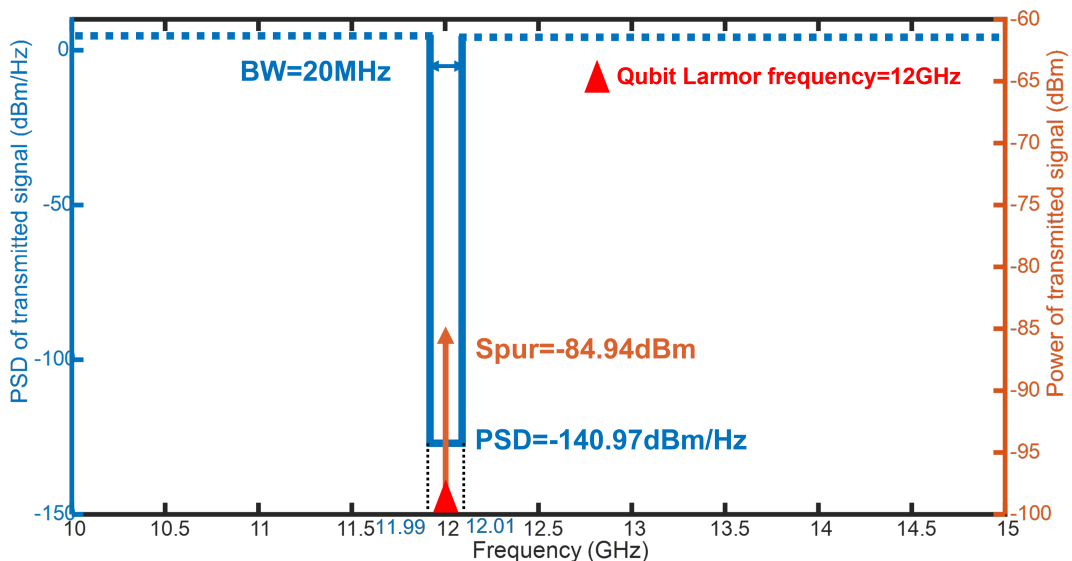


Figure 3.7: Reference of Transmitter Spectrum Mask

Table 3.2: PSD Calculation Parameters and Requirement

<b>PSD Requirement Calculation</b>	
$F'$	$1 \times 10^{-6}$
$\omega_0$	12GHz
$L$	20dB
$R_0$	50Ohm
$k$	$5 \cdot 10^8 [Hz/V]$
$T_{idle}$	10μs
<b>PSD (<math>S_{Tx}(\omega)</math>)</b>	-140.97 [dBm/Hz]
<b>spur (<math>\delta_{spur}</math>)</b>	-84.94[dBm]

### 3.1.4 Conclusion

In this section, the mechanism of interference with qubit is discussed. By theoretical modeling with the qubit spectrum transfer function and infidelity, PSD and spur requirement of the transmitter are derived. Fig. 3.7 summarized the specifications required for spectrum mask with qubit infidelity of  $10^{-6}$ , which provides the reference for the following transmitter specification calculation.

## 3.2 Frequency specification

We consider the following items to select the operating frequency of the cryogenic transceiver.

- As discussed in the previous subsections, the output noise of the classical transmitter at the resonance frequency of the quantum link must be low enough not to affect the fidelity of the quantum processor. Considering the required data rate of 12 Gbps (concluded in 2.2) and employing 64-QAM modulation (see Chapter 5 for more explanation), the transmitter data bandwidth ( $BW_{RF}$ ) is 2 GHz. The transmitter's undesired emission at the first, second, and third adjacent channels is typically limited by the transmitter nonlinearity, and will be relatively large. Consequently, there must be a frequency distance of at least  $4 \times BW_{RF} = 8$  GHz between the operating frequency of the quantum and classical links. In the last project meeting in Dublin, the operating frequency of the quantum link is decided to be  $\sim 20$  GHz considering the dimension of the waveguides connecting different quantum cores. As a result, the operating frequency of the classical link must be either below 12 GHz or above 28 GHz to have a minimum impact on the fidelity of the quantum link.
- Unfortuantely, the size of an on-chip antenna becomes impractically large at an operating frequency below 12 GHz. For example, considering a dielectric constant of 4, and a substrate thickness of  $300 \mu\text{m}$ , the dimension of a patch antenna will be about  $6\text{mm} \times 8\text{mm}$ , 10 times larger than the transmitter core area, thus increasing the system cost significantly. Moreover, it would be extremely challenging to achive such a large data bandwidth at such a relatively low carrier frequency. Consequently, the operating frequency of the classical link should be above 28 GHz.

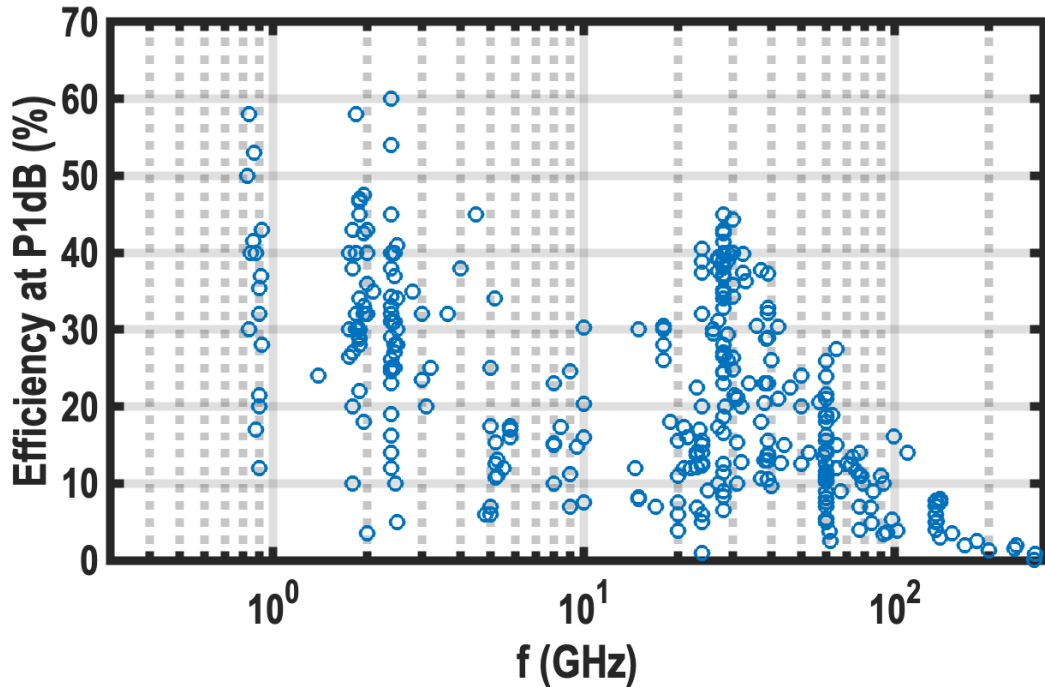


Figure 3.8: Efficiency of state-of-the-art CMOS power amplifiers at their 1-dB power compression points versus their operating frequencies.

- It is worth mentioning that the operating frequency range of cryogenic probe stations of EPFL and TUD labs is below 40 GHz. Consequently, operating at an operating frequency above 40 GHz is not wise and would cause many measurement uncertainties and challenges. .
- Fig. 3.8 shows the efficiency of state-of-the-art CMOS power amplifiers at their 1-dB power compression points versus their operating frequencies. Clearly, the PA efficiency starts dropping significantly at the frequencies above 40 GHz, mainly due to the power gain reduction of CMOS transistors. Since the cooling power of the dilution fridge is limited, the transmitter's efficiency must be maximized, and an operatig frequency of 28-30 GHz is chosen for the classical link.

## 4. Channel model

This chapter provides a first approach for communications in cryogenic temperatures in a quantum package. We summarize the structure design and the possible alterations that could be made to the geometry of the package to provide isolation to the qubits while having a functional traditional wireless channel. All simulations were made using CST MWS [2]. From there, we can proceed to extract the channel and perform its characterization based on path losses and delay spread.

### 4.1 Wireless channel in a computer chip

The base structure to observe the influence of temperature in the wireless channel is a functional flip chip package at a frequency of 60 GHz. We model the first cryogenic channel in this structure because of its simplicity and our previous experience working with it.

The structure is made stacking layers of copper and dielectric. From top to bottom, the layers are heat sink and heat spreader, both to dissipate the heat of the structure because of their thermal conductivity. Follows the silicon die, made of bulk silicon for the operation of transistors. The material of this layer is harmful to the electromagnetic propagation around the package. The insulator layer is made of silicon dioxide ( $\text{SiO}_2$ ), and separates the silicon die from the interconnect layers, which are made of copper [27].

The flip chip is also surrounded by a metallic enclosure. This converts the wireless channel into a reverberation chamber. The energy will bounce around the structure and create notches in the channel response in frequency and time. However, since all the architecture, node placement, and geometry are known beforehand and remain static after implementation, we have the leverage of having an almost deterministic

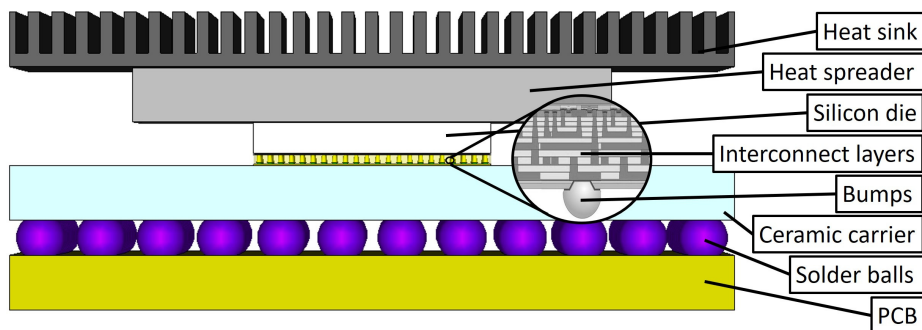


Figure 4.1: Schematic of the layers of a flip-chip package [3].

Table 4.1: Characteristics of the layers in a flip-chip package and default dimensions.  $\epsilon_r$  is the relative permittivity of the material,  $\tan(\delta)$  is the loss tangent, and  $\rho$  refers to the conductivity. PEC stands for perfect electrical conductor (lossless material of infinite conductivity) [36].

	<b>Thickness</b>	<b>Material</b>	$\epsilon_r$	$\tan(\delta)$	$\rho$
Heat sink	0.1–0.5 mm	Aluminum	PEC	PEC	PEC
Heat spreader	0.1–0.5 mm	Aluminum Nitride	8.6	$3 \cdot 10^{-4}$	—
Silicon die	0.5 mm	Bulk Silicon	11.9	—	$10 \Omega \cdot \text{cm}$
Insulator	10 $\mu\text{m}$	$\text{SiO}_2$	3.9	0.025	—
Bumps	87.5 $\mu\text{m}$	Cu and Sn	PEC	PEC	PEC
Redistribution layer	3 $\mu\text{m}$	Copper	PEC	PEC	PEC
PCB	0.5 mm	Epoxy resin	4	—	—

and invariant channel. This knowledge allows an accurate pre-characterization of the channel, easing the compensation tasks of the channel impairments.

For this setting, we compare the channel and the EM propagation for a flip chip at room temperature and the same structure at cryogenic temperatures. Since CST does not take into account temperature when simulating, we must model the behavior at cryogenic temperatures by modifying the characteristics of the materials. Low temperatures influence the electric conductivity and the losses of the materials, while the matter parameters (permittivity and permeability) remain almost constant. The metals will become superconductive and the losses on the silicon and aluminum nitride in the structure will be negligible. Therefore every metal for the structure at 4 Kelvin will be modeled as a perfect electric conductor (PEC), and the dielectrics will be modeled as lossless materials. This approach is not entirely accurate but it provides a fair enough approximation with low computational costs. To perform the EM propagation we use 16 monopole antennas, that are placed through the silicon and feed from the metal layers below.

In Figure 4.2 we can see the difference in the behavior for both setups. It is clear that for room temperatures, the channel will be less notchy, thanks to the lossy nature of the bulk silicon, that absorbs a large portion of the radiation paths. This makes for low delay spread but a largely attenuated channel leading to power deficit in transmission. The opposite occurs when considering the materials as perfect conductors or with negligible losses. The channel becomes notchy and enlarges due to the high amounts of paths bouncing on the structure. In this case, we deal with a reverberant channel with low path losses but enlarged due to the delay spread. In figures 4.2a and 4.2b we can see insets of the EM field for both temperatures. This field distribution matches with what is inferred from the S parameters. In the lossy material, the landscape is almost blue with a small amount of waves going around the geometry. In the other case, we find many spots of field concentration because of the reverberant nature and low path losses given by low temperatures.

This approach has allowed us to have first-hand knowledge of the behavior of the channel at cryogenic temperatures. When moving to a quantum package design, it is expected that the wireless channel will behave similarly.

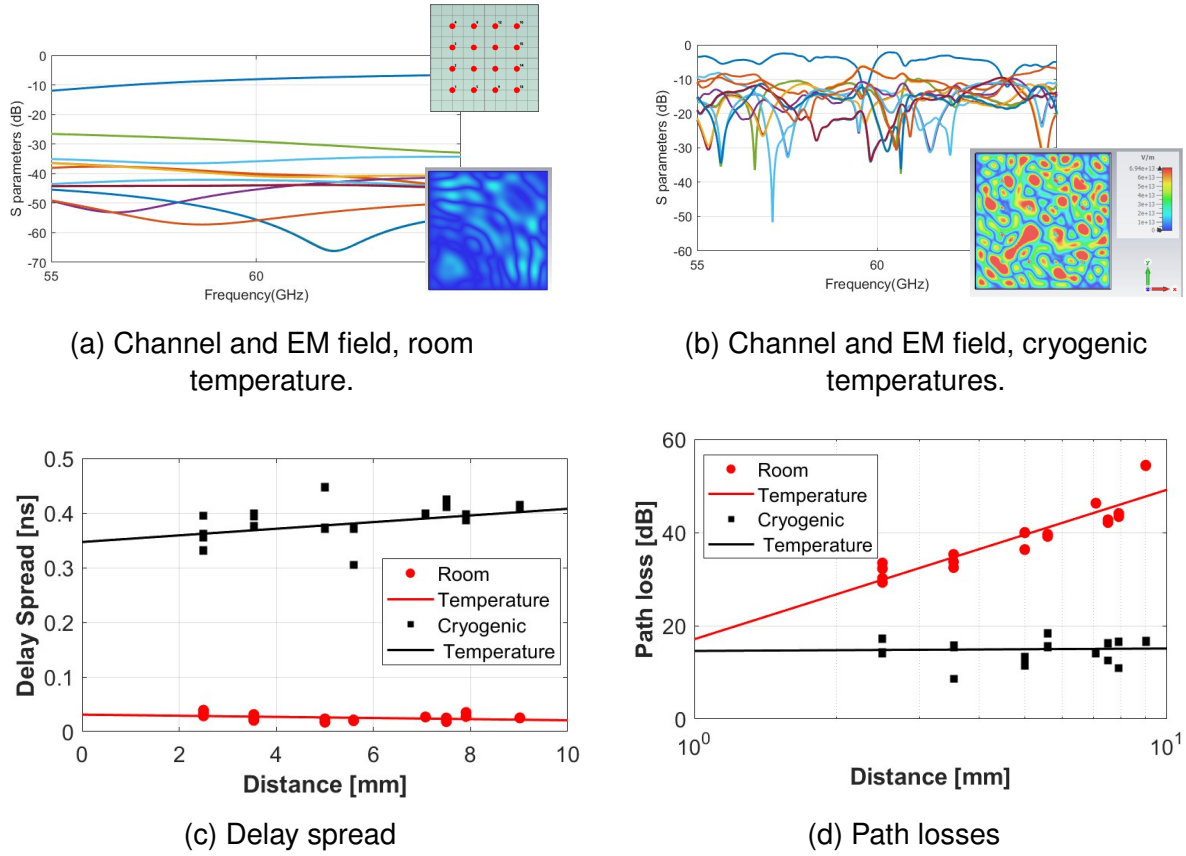


Figure 4.2: Channel behavior and characterization for room and cryogenic temperatures

## 4.2 Quantum package design

Once we know what to expect when transmitting in an almost-perfect environment we proceed to model a geometry of the quantum package based on the structure presented in the proposal, see figure 4.3.

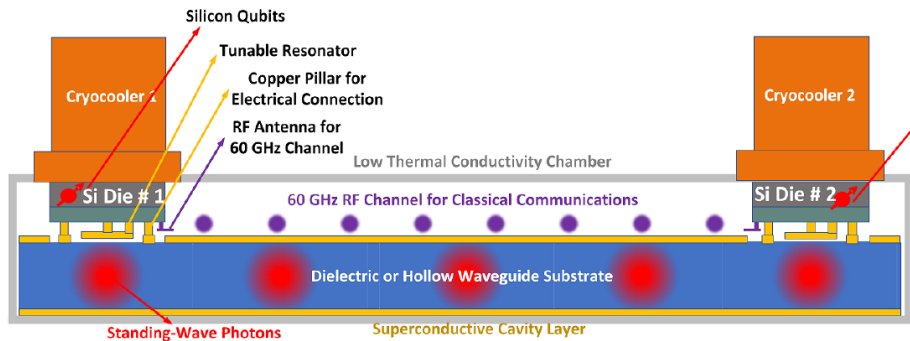


Figure 4.3: Proposal of the quantum cavity

The system requirements for the transceiver design define a frequency of operation of 28 GHz. We adopt this frequency for our wireless channel design. The monopole antenna that was used at 60 GHz is reusable since the new frequency is approximately a harmonic and will radiate properly. The superconductive waveguide for the qubit

transmission will be modeled as a PEC cavity filled with vacuum. We do this to have a more realistic model of what we want, however, our priority is the wireless channel characterization, and we focus on that. Also, isolating the qubit from the channel reverberance is one of our major concerns and we address this with some changes in the design. To simulate transmission in cryogenic temperatures, we repeat the approach explained in the previous section, and model every material as perfect and lossless.

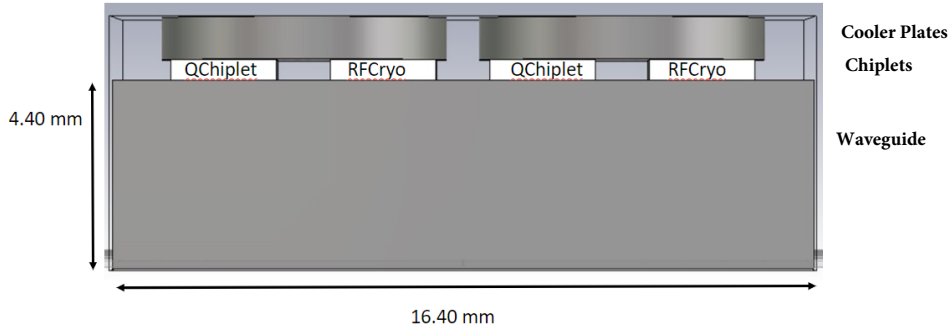


Figure 4.4: Quantum Package in CST

What was simulated in CST can be seen in Figure 4.4. Though this is not seen in the figure, the whole structure is surrounded by a metal cavity filled with vacuum, that covers the chiplets and a portion of the cooler plates. From top to bottom, we have metallic cooler plates (PEC). Next the chiplets, based on the flip chip structure, with two layers, one of silicon, and the other of ( $\text{SiO}_2$ ), both lossless. The last layer represents the superconductive waveguide. Under each cooler plate, we have two chiplets. One of them is exclusively dedicated to passing the qubits to the waveguide (Qchiplet). The other (RFCryo) is augmented with the monopole antenna and used for wireless transmission.

Right under the QChiplet, there is an opening that connects to the inside of the waveguide, which is used for the qubits transit. We place an antenna in the aperture, to measure how the wireless channel radiation will affect the QChiplet, see Figure 4.5a, the antenna in the opening is represented by a red arrow.

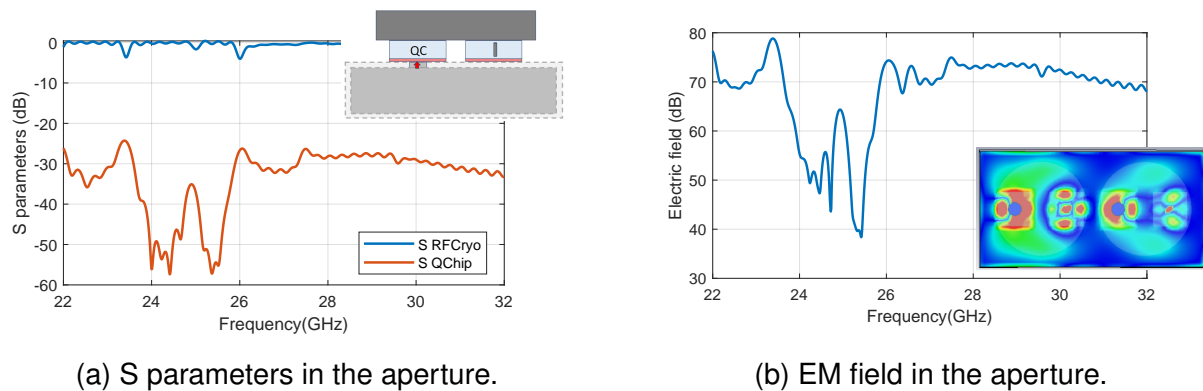
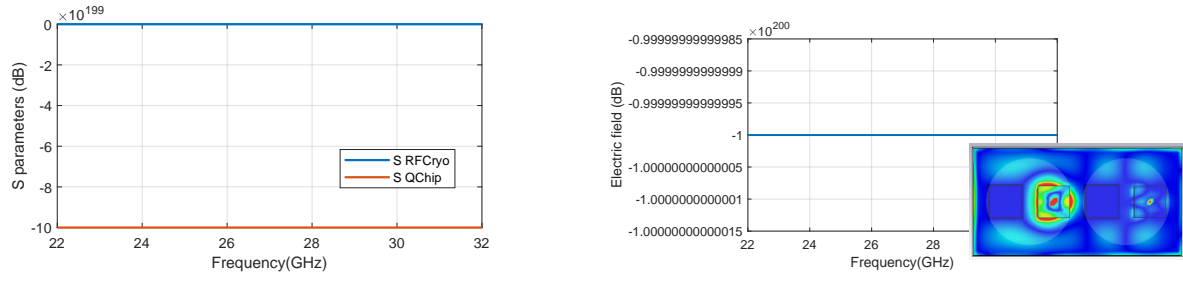


Figure 4.5: Isolation of the QChip

The S parameters shown in Figure 4.5a prove that when the RF antenna radiates, the energy that reaches the aperture is low, and we seem to have decent isolation

values. Moreover, we place a field probe in the aperture to check the amount of EM field that is leaking towards the waveguide see Figure 4.5b. Our results conclude that there is a nice isolation between the QChiplets and the classical wireless channel. However, since the qubits are quite unstable, these values might not suffice and can jeopardize the entire system.

One approach that could improve these values is shielding the entirety of the QChiplet, to reflect unwanted radiation. This alternative was simulated by us in CST see Figure 4.6.



(a) S parameters in the aperture.

(b) EM field in the aperture.

Figure 4.6: Isolation of the QChip

The results show that surrounding the QChiplet with metal has a positive influence on the amount of energy that will leak into the quantum cavity. It is worth mentioning that the notches in frequency and enlargement in time are still present, though not visible in the images due to their values.

### 4.3 Conclusions

We have done full wave characterizations of the system to model a classical wireless channel within a functioning quantum package. Our approach was based on the previous knowledge and work developed on computer chips. First, the characterization was done by assessing how materials deliver and behave in cryogenic temperatures. Moving forward, the materials were used in a structure assumed from the proposal data. Our results prove the reverberant nature of the wireless channel in a quantum package and the isolation possibilities of the Qchiplets.

# 5. Link Budget

As indicated in Table 2.1, achieving a data rate of 12 Gbps would facilitate direct support for an 8-core processor with a fidelity of 99.9%, representing a notable advancement in the field of quantum computing. Considering the limitations imposed by the power budget, the target data rate of the transceiver has been established at 12 Gbps.

This chapter will calculate the cryogenic mmWave transceiver's link budget based on the system-level analysis in Chapter 2 and Chapter 3, as shown in Table 5.1.

Table 5.1: System Requirements

System Requirements	
Maximum data rate(bit rate)	12 Gbps
Operating frequency	28 GHz
Maximum distance	0.1 m

## 5.1 Free Space Path Loss

The distance between the two transceivers is a maximum of 0.1 m, as shown in Fig. 1.1. Firstly, it is important to determine the carrier frequency. Opting for a higher frequency can result in a smaller antenna, but it also leads to more path loss. On the other hand, a lower frequency can achieve less path loss, but it results in a bigger size that is not ideal for scaling the entire system. Therefore, it is crucial to choose a moderate frequency that strikes a balance between antenna size and path loss. Additionally, the influence of leakage signals from the transceiver on the qubit cavity must be carefully evaluated, in line with the detailed analysis presented in Chapter 3. After considering various factors, we have decided to use a carrier frequency of 28 GHz for our application. This particular frequency band is also used for 5G communication and our testing instrument supports it. Additionally, we have ample experience in IC design for this frequency range. The 28 GHz frequency can accommodate a large bandwidth, which is necessary for our application. The size of the single patch antenna is about 4 mm. Lastly, the path loss at this frequency is within acceptable limits. According to equation (5.1), the path loss can be calculated. The free space path loss is 41.4 dB at 28 GHz, as shown in Figure 5.1.

$$FSPL = 20 \log_{10}(d) + 20 \log_{10}(f_c) + 20 \log_{10} \left( \frac{4\pi}{c} \right) \quad (5.1)$$

where d represents the distance,  $f_c$  is the carrier frequency, and c is the speed of light.

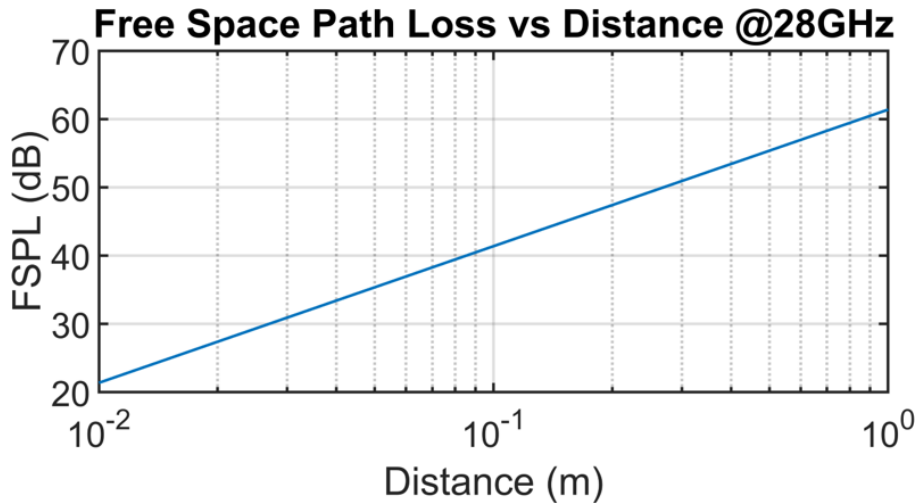


Figure 5.1: Free space path loss at 28 GHz

## 5.2 Selection of Modulation

In order to select the appropriate modulation, it is necessary to consider factors such as multipath effects of wireless signal transmission, inter-symbol interference, and signal bandwidth. For this, it is necessary to introduce the concepts of delay spread and coherent bandwidth.

Similar to commercial wireless communication, multipath propagation effects in quantum computer packages cause signal dispersion due to finite package boundaries. Each path has its own delay, and dispersion in time domain leads to a form of intersymbol interference. Delay spread is an indicator measuring the multipath characteristics of wireless communication channels. It is usually defined as the difference between the arrival time of the earliest arriving component and the arrival time of the latest multipath component. Delay spread is a random variable, and its standard deviation is a common measure for it. This measure is widely known as the root mean square delay spread  $\sigma_\tau$ . Coherent bandwidth  $B_c$  is a statistical measure indicating the frequency range over which the channel can be considered flat. This means that the receiver obtains all spectral components with approximately the same gain and linear phase [15]. All frequency components of the transmitted signal will fade simultaneously within the coherent bandwidth. Coherent bandwidth is inversely proportional to delay spread as equation (5.2).

$$B_c = 1/\sigma_\tau \quad (5.2)$$

Delay spread  $\sigma_\tau$  and coherent bandwidth  $B_c$  are parameters describing the dispersion in time-domain characteristics of wireless channels. Their values relative to the bandwidth  $BW$  of the transmitted signal and the symbol duration  $T_s$  can help determine whether the channel experiences flat fading or frequency-selective fading. In short, if the bandwidth of the transmitted signal is less than the coherent bandwidth, frequency-selective fading caused by delay spread can be neglected.

The dispersion within the quantum computing package can be analyzed through the approximation provided by the chamber model. This model conceptualizes the wireless links as being enclosed within a metallic container. The root mean square

delay spread  $\sigma_\tau$  is calculated using certain material parameters of the chamber. This calculation involves a variety of factors as follows [13]:

$$\sigma_\tau = \frac{1}{2\pi f S_Q} \quad (5.3)$$

Here,  $S_Q$  denotes the aggregate of the reciprocals of the different Q-factors. These factors incorporate considerations for the electromagnetically absorptive materials present, the apertures in the chamber, the conductive properties of the chamber walls, and the dimensions of the antennas. The aperture Q factor becomes relevant only in scenarios where significant openings exist in the chamber walls. Therefore, for calculations pertaining to a package, it is sufficient to include only the wall and antenna-related Q factors [21]. The Q factor associated with the chamber walls is given by

$$Q_{\text{wall}} = \frac{3V}{2\mu_r \delta S} \quad (5.4)$$

and for the antenna, it is defined as

$$Q_{\text{antenna}} = \frac{16\pi^2 V}{m \lambda^3} \quad (5.5)$$

where  $V$  represents the cavity volume ( $d \times d \times h$ ),  $S$  is the surface area ( $2d^2 + 4hd$ ),  $\mu_r = \mu_w/\mu_0$  denotes the relative wall permeability (with  $\mu_w$  as the actual wall permeability and  $\mu_0$ , the permeability of free space),  $m$  is the antenna impedance mismatch factor (assumed to be 1 for a perfect impedance match), and  $\delta$  is the skin depth, calculated as  $1/\sqrt{\pi f \mu_w \sigma_w}$  with  $\sigma_w$  representing the wall conductivity. For materials that are non-ferric, it is standard to assume that  $\mu_w = \mu_0$ .

If we assume the dimensions of the package are  $0.1\text{ m} \times 0.1\text{ m} \times 0.002\text{ m}$ , one can apply equation (5.2)-(5.5) to determine the relationship between the operating frequency, the delay spread and coherent bandwidth, as shown in Fig. 5.2. Given an operating frequency of  $28\text{ GHz}$ , and the corresponding delay spread and coherent bandwidth are  $7.4\text{ ns}$  and  $135\text{ MHz}$ , respectively, it would be advisable for the bandwidth of the transmitted signal to be less than this coherent bandwidth.

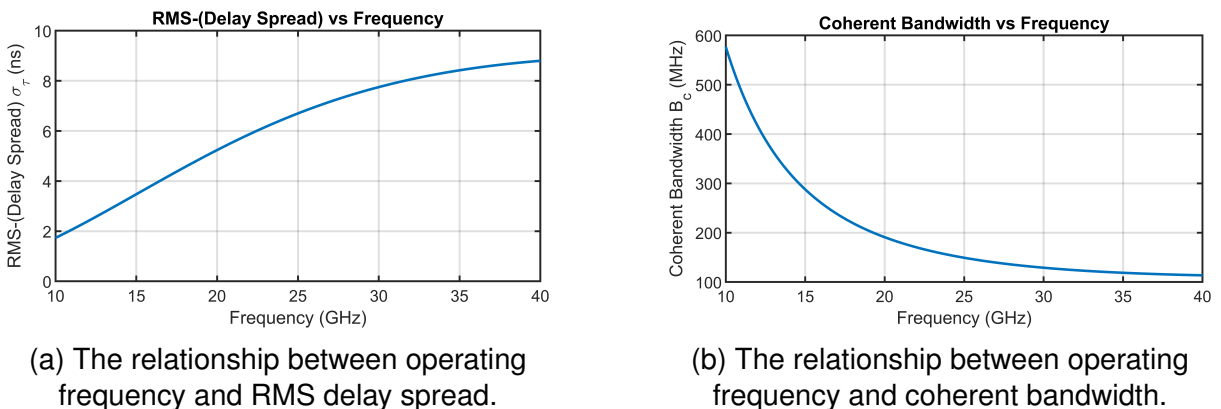


Figure 5.2

With a maximum bit rate of 12 Gbps according to Table 5.1, the relationship between the signal's bandwidth and the data rate could be approximated by the equation (5.6).

$$BW \approx BitRate/\log_2(M) \quad (5.6)$$

where M represents the order of modulation. If a 64-QAM modulation signal is used, the signal bandwidth calculated according to equation (5.6) is approximately 2 GHz. Consequently, the signal is inevitably subject to frequency selective fading. To mitigate this issue, Orthogonal Frequency Division Multiplexing (OFDM) technology can be utilized. This approach is distinct from employing a single carrier with 64-QAM modulation, which necessitates a bandwidth of 2 GHz. Utilizing OFDM with multiple carriers allows for the division of the total 2 GHz bandwidth across several sub-channels. This division ensures that the bandwidth of each sub-channel remains below  $B_c$ , below which frequency selective fading becomes negligible. Therefore, within each sub-channel, the effects of frequency selective fading can be considered negligible. In conclusion, 64-QAM OFDM modulation is a reasonable and feasible modulation scheme.

## 5.3 Sensitivity Calculations

Equation (5.7) provides the sensitivity on the receiver side.

$$\text{Sensitivity} = 10 \log(kT) + NF_{RX} + 10 \log(BW) + SNR_{min} \quad (5.7)$$

where  $T$ ,  $NF_{RX}$ ,  $BW$ ,  $SNR_{min}$  denotes environmental temperature, the noise figure of the receiver, signal bandwidth, and minimum signal-to-noise ratio required by the system. k is Boltzmann constant, is  $1.38 \times 10^{-23} J/K$ .

At a bit-error rate of  $10^{-6}$ , the simulated  $SNR_{min}$  for different modulations in additive white Gaussian noise (AWGN) are shown in Fig. 5.3. The 64-QAM signal stipulates a minimum Signal-to-Noise Ratio (SNR) of 27 dB, positioned between the SNR requirements for 4-QAM and 256-QAM.

The estimated noise figure of the receiver in this frequency is 5 dB at room temperature [38] [20]. However, the transceiver in QUADRATURE project operates at 4K. The noise figure and thermal noise  $kT$  are lower than those at room temperature. To estimate the noise figure at 4K, the concept of noise temperature is introduced. The relation between noise figure and noise temperature is shown in the equation (5.8). At room temperature, the noise figure of 5 dB is converted to a noise temperature of 627.1 K. This temperature then decreases by a factor of four [34], resulting in an expected  $T_{Noise}$  of 156.8 K. Finally, the expected noise temperature needs to be converted to noise figure at  $T_{Ref}$  of 4K to calculate the sensitivity. The calculated sensitivity is  $-56.6 \text{ dBm}$  at 4K and  $-49.0 \text{ dBm}$  at room temperature.

$$\begin{aligned} T_{Noise} &= T_{Ref} \times \left( 10^{\frac{NF(dB)}{10}} - 1 \right) \\ NF(dB) &= 10 \times \log\left(\frac{T_{Noise(K)}}{T_{Ref(K)}} + 1\right) \end{aligned} \quad (5.8)$$

## 5.4 Output Power and EVM<sub>TX</sub>

After obtaining the sensitivity requirements of the receiver, the required output power can be calculated according to the equation (5.9).

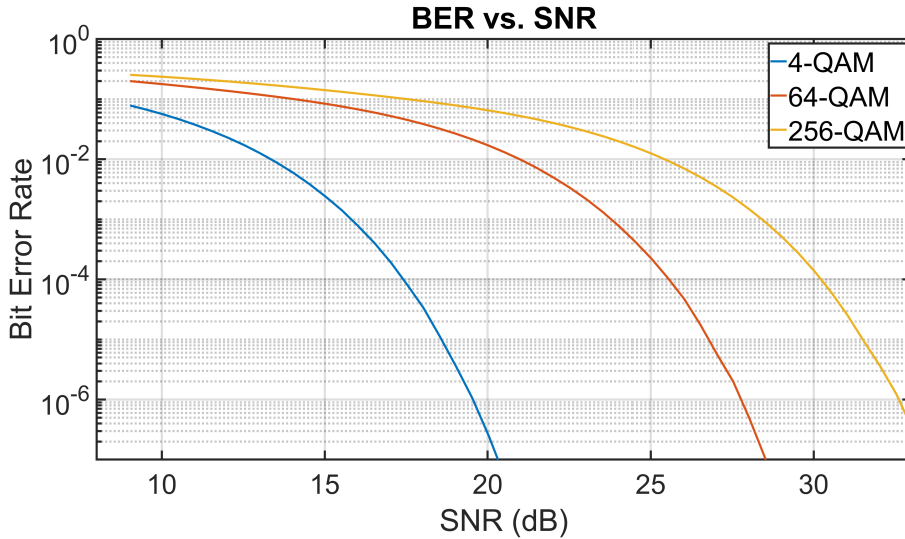


Figure 5.3: BER vs. SNR

$$P_{RX} = P_{TX} - FSPL - \text{Implementation Loss} + G_{TX} + G_{RX} \quad (5.9)$$

$$\text{The Required Output Power} \geq P_{TX} + \text{PAPR} + \text{margin} \quad (5.10)$$

where  $P_{RX}$ ,  $P_{TX}$ ,  $G_{Tx}$ ,  $G_{Rx}$  represent the received signal power at the receiver, the transmitter output power, the transmitter antenna gain, and the receiver antenna gain.  $P_{RX}$  should equal or be larger than the sensitivity to ensure the effectiveness of signal reception. The antenna gain  $G_{TX}$ ,  $G_{RX}$  are 3 dBi [20]. Implementation loss is around 6 dB, including the loss of transmitter to antenna and antenna to receiver. According to equation (5.9), the calculated  $P_{TX}$  is  $-15.2 \text{ dBm}$ .

Furthermore, the required output power of the transmitter is defined in equation (5.10), wherein PAPR denotes the peak-to-average power ratio of signals. Disregarding pulse shaping, the PAPR for a 64-QAM signal is quantified at  $3.7 \text{ dB}$ . A margin of  $10 \text{ dB}$  is adopted, considering the potential employment of orthogonal frequency division multiplexing (OFDM) modulation technique, which is known to induce a higher PAPR. Therefore, to ensure a robust link, the transmitter's output power should deliver  $-1.5 \text{ dBm}$  output power.

Another critical metric for the transmitter is the error vector magnitude (EVM), which quantifies the deviation of the transmitted signal from the ideal reference signal. Factors such as the transmitter's internal noise and distortion can degrade the EVM. Moreover, EVM has an approximate mathematical correlation with the SNR, which can be expressed as an equation (5.11). The receiver stipulates a minimum SNR of  $27 \text{ dB}$ , and with an estimated noise figure for the receiver at  $5 \text{ dB}$ , this leads to a derived threshold where the transmitter's EVM must not exceed  $-32 \text{ dB}$  for acceptable performance.

$$SNR = -20\log(EV M_{RMS}) \quad (5.11)$$

## 5.5 Conclusion

Based on the system-level analysis and the system-level requirements obtained from the first two chapters, by calculating and analyzing the path loss, modulation, and receiver sensitivity, the final requirements, such as the transmitted signal EVM, transmitter power requirements, transceiver bandwidth requirements, and receiver noise figure are obtained, as shown in Table 5.2.

Table 5.2: Link budget

<b>Link budget</b>	
$EVM_{TX}$	$\leq -32 \text{ dB}$
$Bandwidth$	$\geq 2 \text{ GHz}$
$P_{out}$	$\geq -1 \text{ dBm}$
Modulation	64-QAM OFDM
$RX_{NoiseFigure}$	$\leq 5 \text{ dB}$

## 6. Mapping the specifications on the transmitter design

Through the calculation of the link budget in the previous chapters, the requirements of the transmitter, such as the EVM of the transmitted signal, output signal power, signal modulation method, and bandwidth, have been determined. This chapter will analyze the specific parameter requirements of the transmitter design.

A conventional I/Q transmitter consists of two signal pathways that are orthogonal to each other: the in-phase (I) component and the quadrature (Q) component. The transmitter's output signal,  $\text{RFout}$ , is the composite of these two components. In this structure,  $X_{BB,I}$  represents the baseband signal in the In-phase (I) path, and  $X_{BB,Q}$  denotes the baseband signal in the Quadrature-phase (Q) path.  $\omega_c$  is the carrier frequency, which is typically much higher than the working frequency of the baseband. These signals undergo up-conversion in a mixer, culminating in the final output of the RF signal, which is defined by  $\text{RF}_{out} = X_{BB,I} \times \cos(\omega_c t) - X_{BB,Q} \times \sin(\omega_c t)$ .

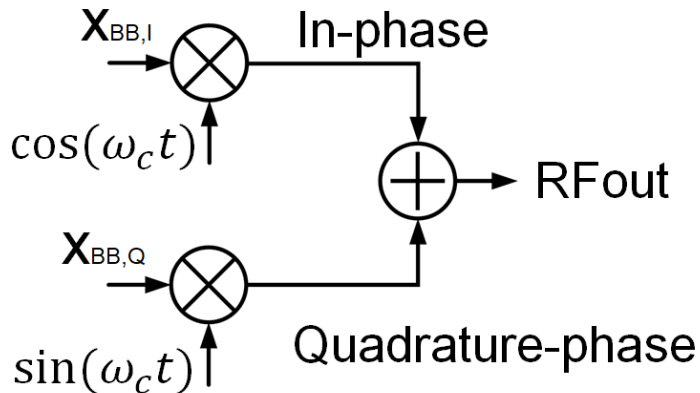


Figure 6.1: Conventional I/Q transmitter block diagram

For the analysis of complex signals including both in-phase and quadrature-phase components, the employment of a constellation diagram is essential, as depicted in Fig. 6.2a. The x-axis symbolizes the in-phase signal, while the y-axis corresponds to the quadrature-phase signal. In the case of an ideal output signal, the blue reference symbol in Fig. 6.2b should occupy the precise intended position. However, actual symbols, due to noise or distortion, might stray from the ideal positions on the constellation, as illustrated by the red measured symbol in Fig. 6.2b. This displacement, termed as the error vector, quantifies the deviation of a symbol on the constellation diagram. Summing all the error vectors yields the error-vector-magnitude, as defined by equation (6.1), where  $N$  denotes modulation order and  $N_{itr}$  denotes the number of iterations for each point.

EVM is an essential specification for the quality of the transmitted signal. It is a parameter used to evaluate the fidelity of a signal in communication systems, denoting the variance from the actual transmitted signal to the idealized one.

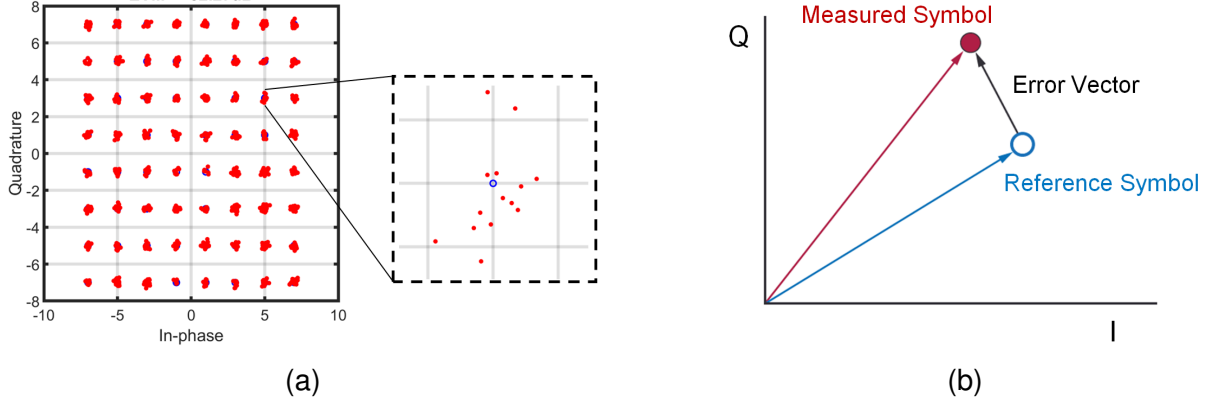


Figure 6.2: Constellation Diagram

$$EVM_{RMS} = \frac{\sqrt{\sum_{i=1}^N \frac{1}{N_{itr}} (e_{ref}(i) - e_{meas}(i))^2}}{\sqrt{\sum_{i=1}^N \frac{1}{N_{itr}} (e_{ref}(i))^2}} \quad (6.1)$$

Various factors can contribute to a symbol's displacement from its ideal location, subsequently degrading the EVM, shown as Fig. 6.3. These include quantization noise emanating from digital-to-analog converters, phase noise arising from the local oscillator, leakage known as LO feedthrough (LOFT), the mismatch between the In-phase (I) and Quadrature-phase (Q) path, and the non-linear characteristics of the power amplifier. It's worth noting that group delay variations, which mainly come from filters, can have a significant adverse effect on EVM due to the transmitter's operation over a wide bandwidth. Moreover, since the factors contributing to the degradation of the EVM are unrelated, the cumulative EVM for the transmitter can be represented by the equation (6.2), where  $EVM_{QN}$ ,  $EVM_{PN}$ ,  $EVM_{LOFT}$ ,  $EVM_{IQmis}$ ,  $EVM_{PA}$ ,  $EVM_{GDV}$  respectively represent the deterioration of EVM caused by DAC quantization noise, phase noise of the local oscillator, feedthrough of the local oscillator, I/Q mismatch, non-linearity of PA, and group delay variation in the transmitter. Regarding the design of the transmitter, key performance indicators, including I/Q mismatch, LO feedthrough, the nonlinearity of the PA, and variations in group delay, are of significant importance. Consequently, this section is dedicated to a detailed analysis of these aspects.

$$EVM_{TX} = \sqrt{EVM_{QN}^2 + EVM_{PN}^2 + EVM_{LOFT}^2 + EVM_{IQMis}^2 + EVM_{PA}^2 + EVM_{GDV}^2} \quad (6.2)$$

## 6.1 I/Q Mismatch and LO Feedthrough

In radio transceiver design, the direct-conversion architecture, shown in Fig. 6.4, is popular due to its simplicity and flexibility. However, this design is prone to the inherent mismatch between the in-phase (I) and quadrature (Q) signal paths. Particularly at

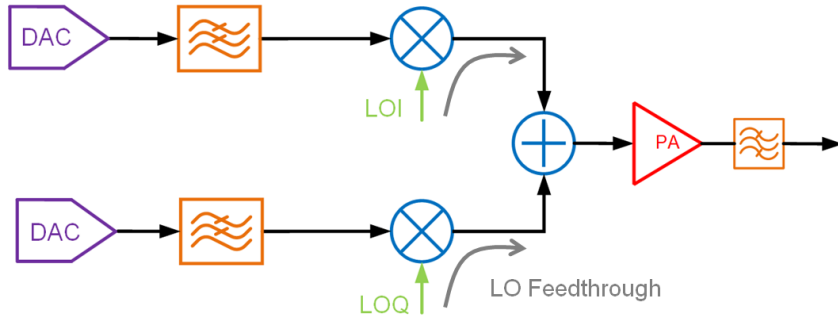


Figure 6.3: Conventional I/Q transmitter block diagram and

millimeter-wave frequencies, the parasitic effects of interconnections, mismatches in electronic components, and elevated frequencies of the local oscillator are likely to result in substantial phase mismatch  $\Delta\theta$  and amplitude mismatch  $\epsilon$ . These mismatches, which are unavoidable in practical implementations, lead to insufficient suppression of image signal [6], creating interference, as shown in Fig. 6.5. Moreover, as a result of the influences of  $\Delta\theta$  and  $\epsilon$ , the output signal  $RF_{out}$  is obtained, expressed as equation (6.3). These mismatches lead to a displacement of the actual transmitted symbol from its ideal position, as depicted in Fig. 6.6. Therefore, such I/Q mismatches can significantly degrade the EVM performance of the transmitter. In order to obtain the relationship between phase mismatch, amplitude mismatch, and EVM as shown in Fig. 6.7, where the x-axis represents the magnitude of phase mismatch, the y-axis represents the magnitude of amplitude mismatch, and the contours in the graph indicate the magnitude of EVM. For example, to achieve as small an EVM value as possible, one can choose the green and blue areas in the graph. To achieve an EVM less than -40 dB, the amplitude mismatch needs to be less than 0.2 dB, and the phase mismatch needs to be less than  $1^\circ$ . In the direct-conversion modulators, the I/Q transmitter's analog baseband circuitry exhibits DC offsets. These offsets in the I and Q paths can lead to leakage of the LO signal into the RF output, thereby contributing additional LO power in direct upconversion transmitters. On the constellation diagram, LOFT manifests as horizontal and vertical shifts, as depicted in Fig. 6.8. This LOFT consequently worsens EVM performance. The degradation of the EVM caused by LO feedthrough can be described by the equation (6.4), where  $P_{LO, leak}$  refers to the power of the local oscillator signal that leaks into the output, and  $P_{OUT, avg}$  is the average output power.

Furthermore, the leaked LO signal can potentially cause interference in adjacent channels, as illustrated in Fig 6.5.

$$RF_{out} = X_{BB,I} \left( 1 + \frac{\epsilon}{2} \right) \cos \left( \omega t + \frac{\Delta\theta}{2} \right) - X_{BB,Q} \left( 1 - \frac{\epsilon}{2} \right) \sin \left( \omega t - \frac{\Delta\theta}{2} \right) \quad (6.3)$$

$$EVM_{LOFT} = \sqrt{\frac{P_{LO, leak}}{P_{OUT, avg}}} \quad (6.4)$$

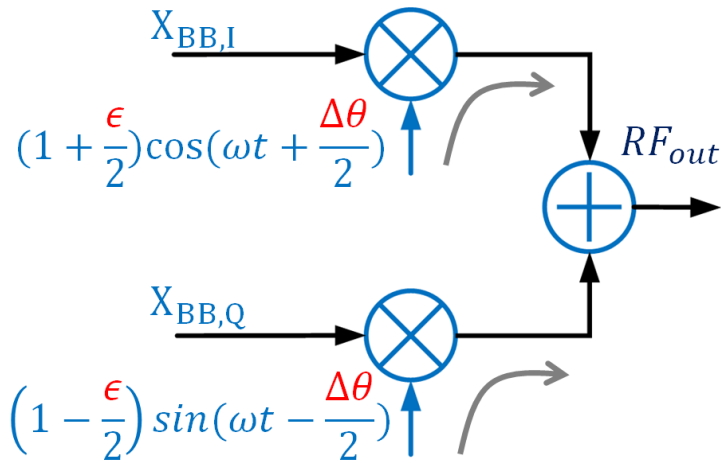


Figure 6.4: I/Q mismatch in direct-conversion transmitter

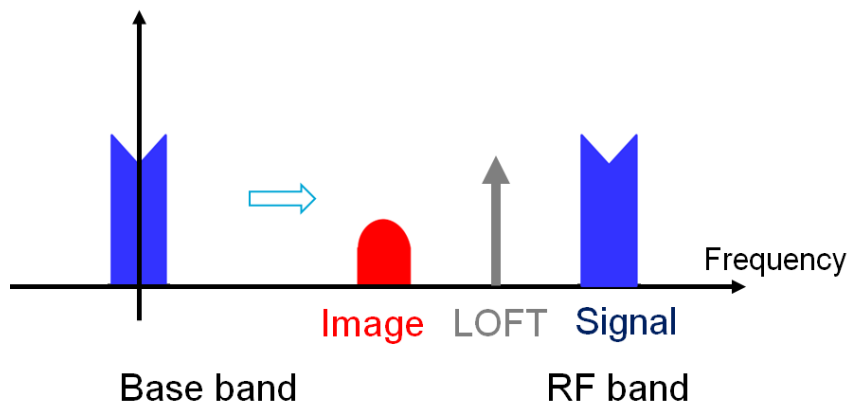


Figure 6.5: Image and LO feedthrough in direct-conversion transmitter

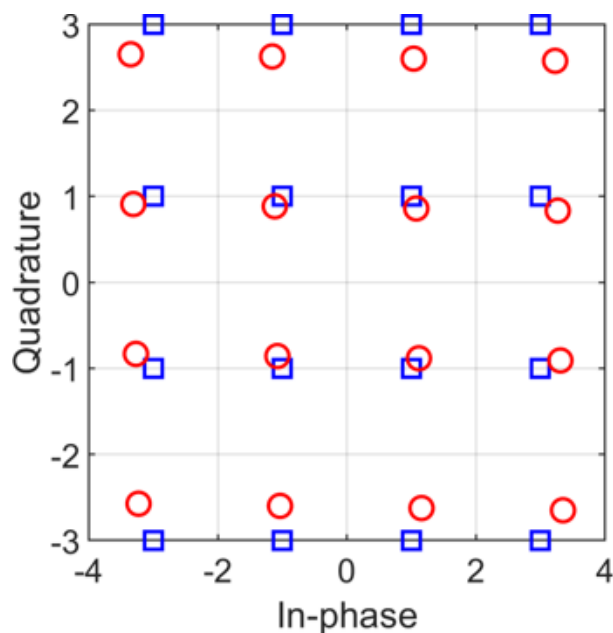


Figure 6.6: Impact of I/Q mismatch in constellation diagram

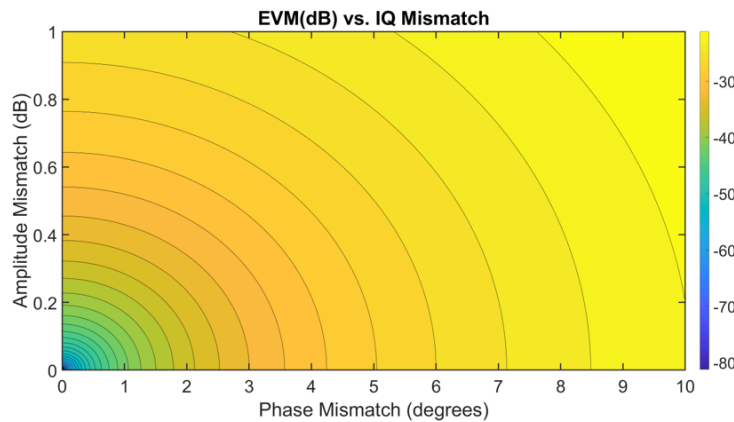


Figure 6.7: The relation between I/Q mismatch and EVM(dB)

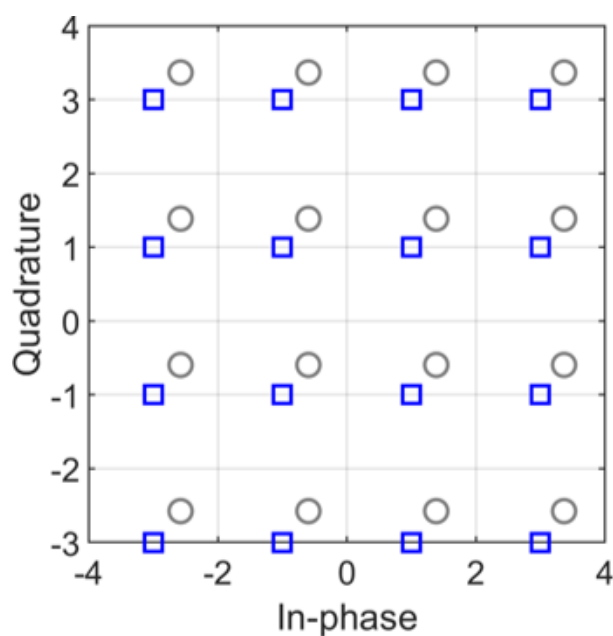


Figure 6.8: Impact of LO feedthrough in constellation diagram

## 6.2 Power Amplifier Non-linearity

In conventional transmitter designs, the primary form of nonlinearity is Power Amplifier (PA) Amplitude Modulation to Amplitude Modulation (AM/AM) compression. This type of compression affects the magnitude of the combined In-phase (I) and Quadrature (Q) signals. At the PA input, the input symbol is  $u(t) = I\cos(\omega t) - Q\sin(\omega t)$ , and its magnitude and phase of each symbol is  $A = \sqrt{I^2 + Q^2}$  and  $\phi = \tan^{-1}(\frac{Q}{I})$ . Considering a classic differential amplifier as shown in Fig. 6.9a, as  $V_{in}$ 's amplitude increases, when  $V_{in+}$  becomes significantly more positive compared to  $V_{in-}$ , transistor M1 is "on", while M2 is turned off. The entire current from the current source  $I_{SS}$  is directed towards M1, resulting in  $V_{out+}$  equalling  $V_{DD}$  minus  $I_{SS}$  times  $R_D$ , and  $V_{out-}$  equalling  $V_{DD}$ . Consequently,  $V_{out}$  becomes  $-I_{SS}R_{DD}$  under these conditions. Conversely, when  $V_{in-}$  is significantly more negative than  $V_{in+}$ , V<sub>out</sub> becomes  $+I_{SS}R_{DD}$ . Thus, with increasing the amplitude of  $V_{in}$ , the output  $V_{out}$  fails to achieve the desired amplification, as depicted by the blue dashed line in Fig. 6.9b. Instead, a clipped red curve is observed. Owing to the differential nature of the circuit, only even harmonic components are relevant. The output voltage for AM/AM distortion is described by equation (6.5), where  $a_1$  is the linear gain,  $a_3$  is the third term related to PA AM/AM distortion.

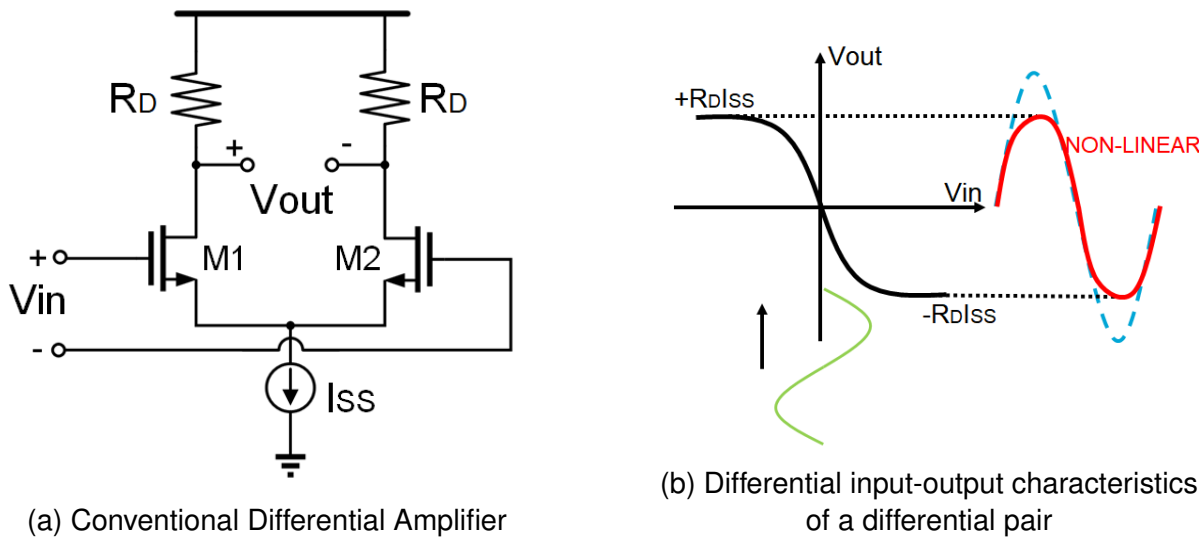


Figure 6.9: PA AM/AM Distortion

$$y(t) = a_1 u(t) + a_3 u^3 \quad (6.5)$$

Fig. 6.10a illustrates the concept of the 1dB compression point. This point is defined as the level of input signal at which the gain decreases by 1 dB. When the relationship between the input and output levels is plotted on a log-log scale, the output level, denoted as  $P_{out}$ , is observed to be 1 dB below its ideal linear response at the 1dB compression point. Within the nonlinear model represented by equation (6.5), this specific 1 dB compression point is quantified as  $P_{in,1dB} = \sqrt{0.145 \left| \frac{a_1}{a_3} \right|}$ , and  $OP1dB = P_{in,1dB} + 20\log(|a_1|) - 1$ .

Furthermore, the output signal tends towards greater linearity as the input signal decreases below the OP1dB threshold. The term 'Power back-off (PBO)' is defined

as  $PBO = OP1dB - P_{out}$ . The relationship between power back-off and the EVM is delineated by equation (6.6), wherein 'C1' denotes a constant value that correlates with the modulation scheme. (For instance, 'C1' is  $6.9\text{ dB}$  for 64-QAM and  $8\text{ dB}$  for 16-QAM.) As shown in Fig. 6.10, an increase in power back-off is correlated with an improvement in EVM. To achieve  $-40\text{ dB}$  EVM, a power back off of  $13\text{ dB}$  is required.

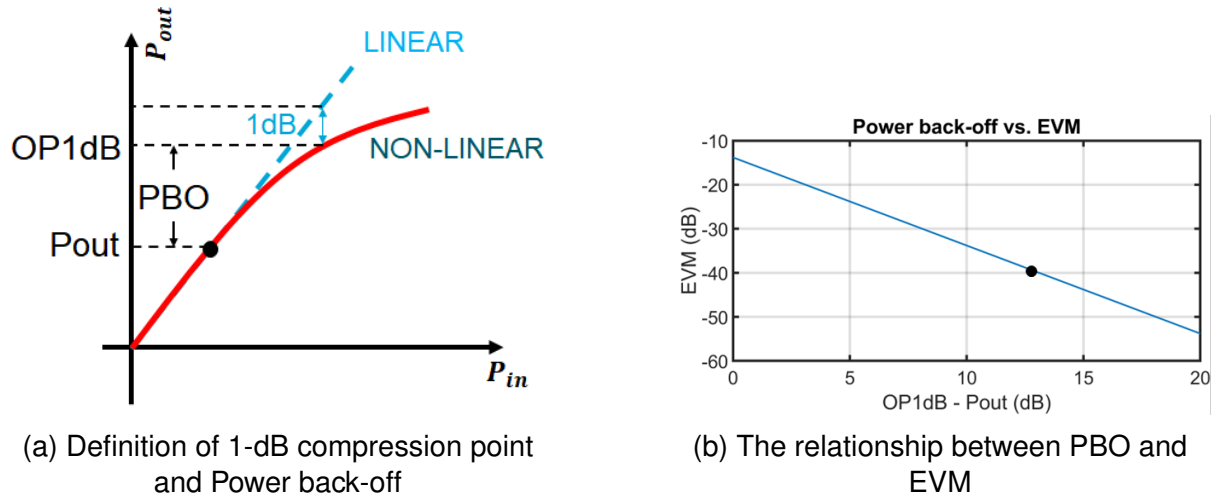


Figure 6.10

$$EVM(\text{dB}) = -2(OP1dB - P_{out} + C1) \quad (6.6)$$

Amplitude Modulation to Phase Modulation (AM/PM) conversion can be understood as the dependency of the phase shift on the signal amplitude. Essentially, for an input signal represented as  $u = Ae^{j\phi_0}$ , the fundamental output component can be described by  $y = Ae^{j(\phi_0+\Phi)}$ , and the AM/PM conversion is determined by equation (6.7), where  $A$  is the input amplitude, and  $c_2$  and  $c_4$  is the coefficient determined by circuit. This implies that AM/PM conversion is likely to occur in systems that exhibit both dynamic and nonlinear characteristics. While AM-AM conversion is typically a result of compression in amplifier gain, amplitude-dependent phase distortion, or AM-PM, may begin to occur even prior to the onset of gain compression.

In the case of the transistor depicted in Fig. 6.11, the main parasitic capacitances are  $C_{gs}$  and  $C_{ds}$ . Variations in  $V_{in}$  result in corresponding fluctuations in  $C_{gs}$  and  $C_{ds}$ , as illustrated in Fig. (6.12). It is evident that the variations in the values of  $C_{gs}$  and  $C_{ds}$  are contingent upon the amplitude of the input signal. Importantly, these variations are not symmetrical with respect to a specific value, denoted as  $C_0$ . This asymmetry introduces an input-dependent term to the phase shift of the fundamental frequency component [35].

$$\Phi = c_2A^2 - c_4A^4 \quad (6.7)$$

To derive the coefficients  $c_2$  and  $c_4$ , it is necessary to perform a large-signal, AC simulation that yields the phase relationship between the input voltage and output voltage, as depicted in Fig. 6.13. Subsequently, these simulation results must be fitted using a specific formula. This process ultimately facilitates the determination of the values for  $c_2 = 1.3755$  and  $c_4 = 3.7644$ . Hence, the equation that defines the relationship between AM/PM can be ascertained. Subsequently, it becomes imperative to

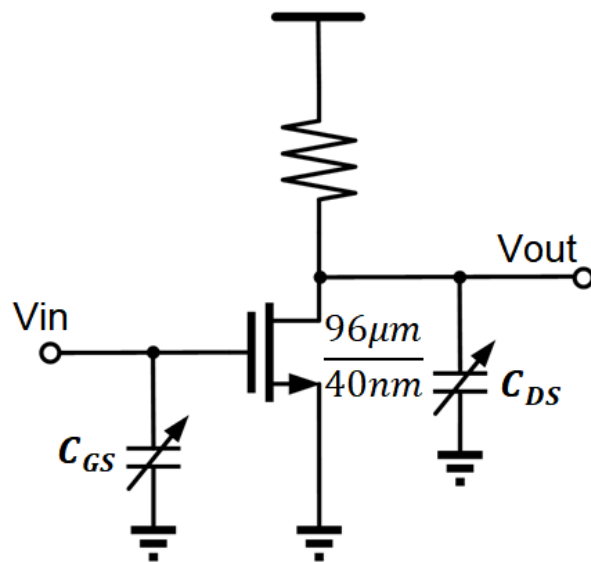
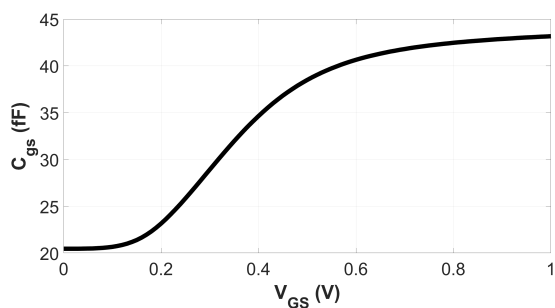
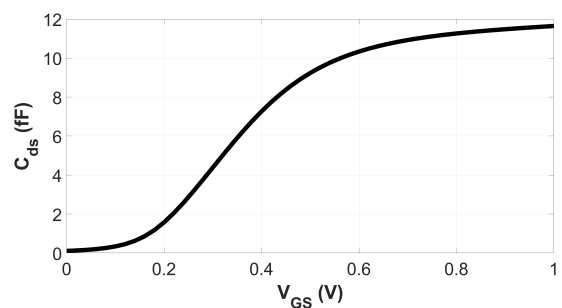


Figure 6.11: Common source stage with parasitic capacitance



(a) The relationship between  $C_{GS}$  and  $V_{GS}$



(b) The relationship between  $C_{DS}$  and  $V_{GS}$

Figure 6.12

investigate the correlation between PM distortion and EVM. As depicted in Fig. 6.14a, research can commence with a 16-QAM signal. Owing to the complete symmetry of the constellation diagram, it is pragmatic to consider only one quadrant initially to reduce computational complexity.

On the constellation diagram, each point exhibits distinct PM distortion due to varying amplitudes. As shown in Fig. 6.14a, point 1 manifests the lowest amplitude, whereas point 4 possesses the highest amplitude, consequently resulting in the greatest deviation angle, denoted as  $\Phi_{max}$ . For a given modulated signal, there exists a definitive relationship between  $\Phi_{max}$  and the deviation angles  $\Phi$  of other points. This relationship allows for the derivation of equation 6.8, which defines the correlation between EVM and  $\Phi_{max}$ . In equation (6.8),  $C2$  is also a value related to modulation. For a 16-QAM signal,  $C2$  equals 7.2; for a 64-QAM signal,  $C2$  equals 9.1. As depicted by Fig. 6.14b,  $\Phi_{max}$  is achieved at the peak output power, denoted as  $P_{peak}$ . In order to maintain the integrity of the output signal, it is customary to set the peak power,  $P_{peak}$ , below the output 1 dB compression point (OP1dB) to prevent distortion which could compromise signal quality.

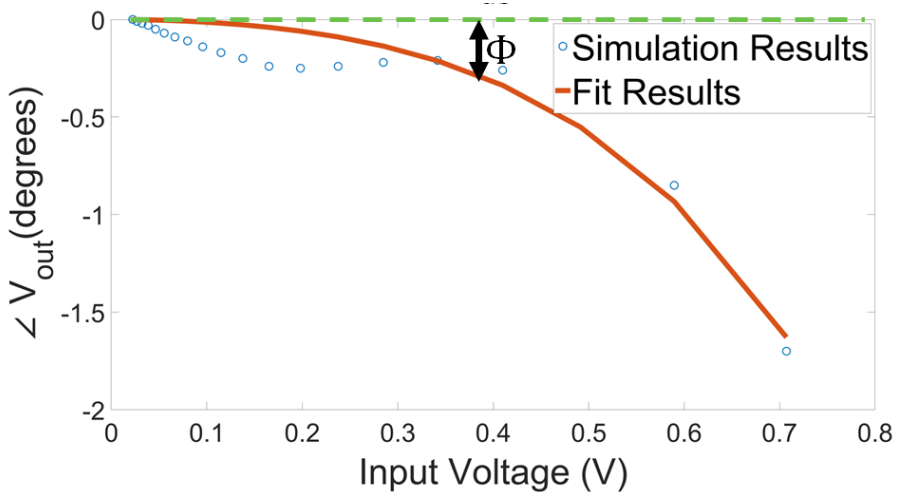
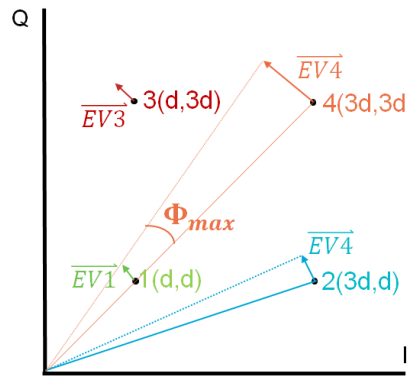


Figure 6.13: The relationship between input voltage and phase of output

$$EVM(dB) \approx 20 \log(|\Phi_{max}|) - C2 \quad (6.8)$$

Fig. 6.15a illustrates the correlation between  $\Phi_{max}$  and EVM, demonstrating a close alignment between theoretical predictions (represented by the red line) and simulation outcomes (depicted by the blue line). Notably, when  $\Phi_{max}$  reaches  $1.4^\circ$  degrees, the EVM is measured at -40 dB, indicative of the signal quality, with the corresponding constellation diagram presented in Fig. 6.15b. This diagram further reveals that points on the outer edges of the constellation experience significant phase deviation, in contrast to the nearly invariant phase of points located towards the center. This observation underscores the differential impact of phase modulation distortion across the constellation.

The previous analysis distinguishes between two types of nonlinearities, AM/AM and AM/PM, and examines them separately. However, these distortions often occur simultaneously, requiring a comprehensive approach as shown in equation (6.9). Linear gain is normalized to 0 dB in this simulation. Coefficients  $c_2$  and  $c_4$  are valued



(a) AM/PM distortion in constellation diagram

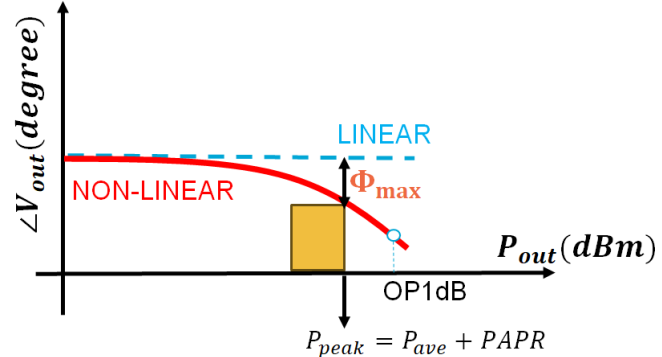
(b) The relationship between AM/PM distortion and  $P_{out}$ 

Figure 6.14

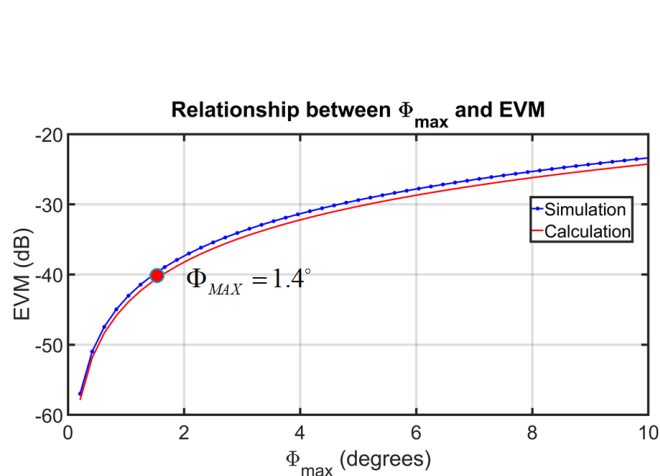
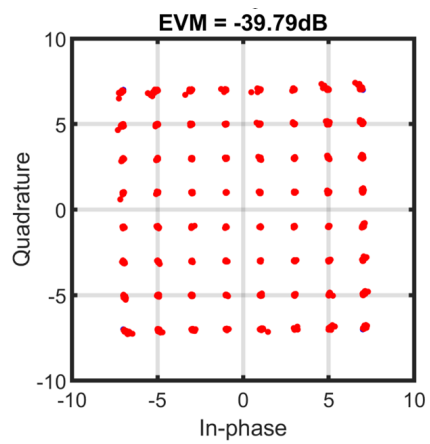
(a) The comparison of simulation and calculation results between  $\Phi_{max}$  and EVM.(b) The constellation diagram simulation results when  $\Phi_{max} = 1.4^\circ$ 

Figure 6.15

at 1.3755 and 3.7644, respectively. This approach facilitates deriving the relationship between OP1dB and EVM as shown in Fig. 6.16. For an output power of  $-1\text{ dBm}$  under 64-QAM modulation, achieving an EVM lower than  $-40\text{ dB}$  requires an OP1dB exceeding  $12\text{ dBm}$ , concurrently maintaining  $\Phi_{max}$  at less than  $1^\circ$ .

$$\begin{aligned}y &= (a_1 + a_3|u|^2) ue^{i\Phi} \\ \Phi &= c_2 A^2 - c_4 A^4\end{aligned}\quad (6.9)$$

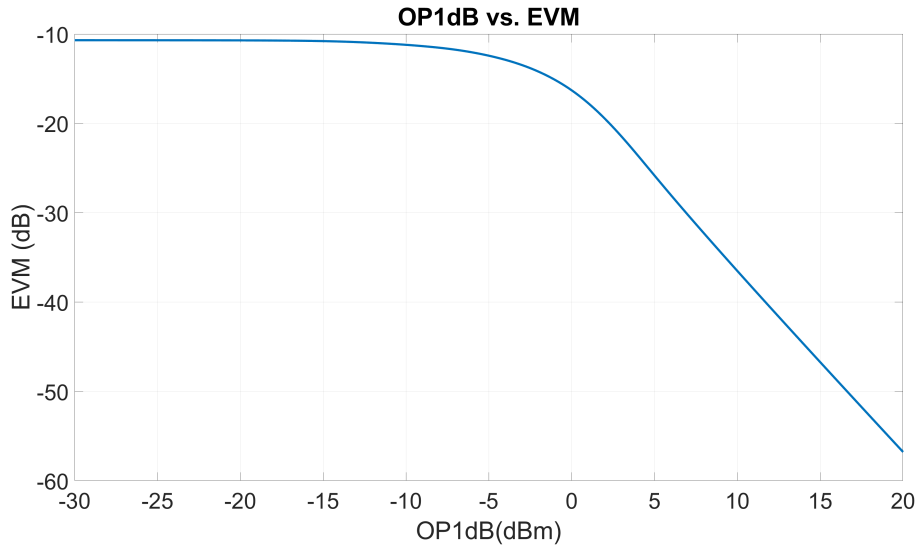


Figure 6.16: The relationship between OP1dB and EVM when using a 64QAM signal with an output power of  $-1\text{ dBm}$ .

## 6.3 Group Delay Variation

The transmitter processes the signal by filtering, up-converting, and amplifying the signal generated at the baseband, as illustrated in Fig. 6.17. The journey of the baseband signal through the transmitter involves various components, including filters, mixers, and amplifiers. The transformation of the signal from baseband to RF band can be summarized as equation (6.10). The value of  $\phi(f)$  changes with the frequency, which is illustrated in Fig. 6.17. The phase shift may display linearity in band, similar to the blue dashed line shown in Fig. 6.17. However, a more prevalent scenario is a nonlinear relationship, as indicated by the red solid line in Fig. 6.17. This nonlinearity primarily arises from the filtering process, with circuit elements like inductance and capacitance further contributing to nonlinear phase shifts.

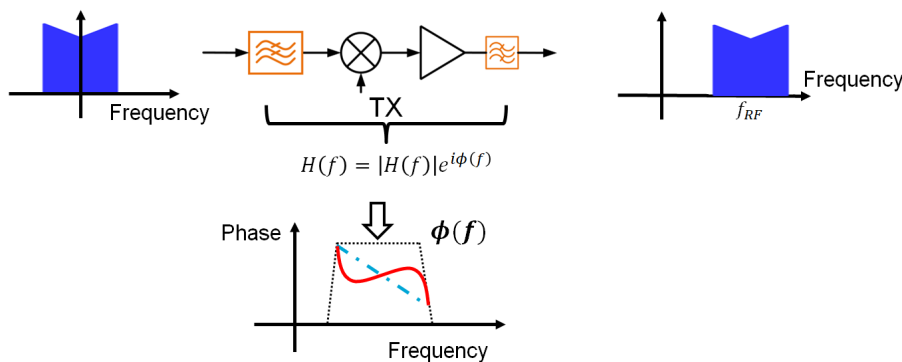


Figure 6.17: Phase shift in transmitter

$$H(f) = |H(f)|e^{i\phi(f)} \quad (6.10)$$

The influence of nonlinear phase shifts on signals in the frequency domain is illustrated in Fig. 6.18. Here,  $f_1$  and  $f_2$  represent components of the signal at different frequencies in the band, each subject to phase shifts that correlate with their frequencies. To fully investigate the impact of nonlinear phase shifts on signal transmission, it is necessary to perform a time domain analysis, as shown in Fig. 6.19. As shown in Fig. 6.19a, the input signal consists of two frequency components,  $f_1$  and  $f_2$ . When a linear phase shift is applied to the input signal, the scenario in Fig. 6.19b is produced. This illustration showcases how linear phase shifts result in uniform delays across frequencies, thereby preserving the signal's integrity. On the other hand, Fig. 6.19c displays the outcome of a nonlinear phase shift, where the delays affecting  $f_1$  and  $f_2$  vary, leading to signal distortion. This analysis highlights the critical difference between linear and nonlinear phase shifts and their impact on signal.

The preceding segment provided a qualitative overview of nonlinear phase shifts. In order to quantitatively analyze the impact of non-linear phase shift on signals, it is necessary to introduce the concept of group delay. As shown in Fig. 6.20a, the diagram explains the relationship between in-band phase shifts and frequency. Deriving group delay from this relationship involves differentiating the phase with respect to frequency, as depicted in equation (6.11). This differentiation quantifies the group delay, illustrating how different frequency components in a signal experience different time delays.

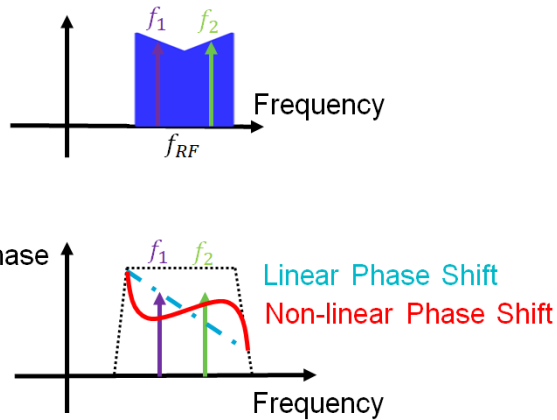


Figure 6.18: Impact of non-linear phase shift in the frequency domain.

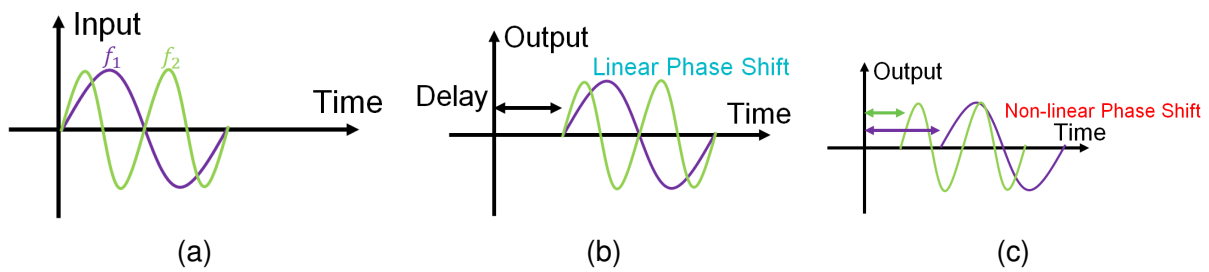


Figure 6.19: Impact of non-linear phase shift in the time domain.

The dependency of group delay on frequency is presented in Fig. 6.20b. For nonlinear phase shifts, represented by the red curve, two key parameters emerge: the average delay, which is the mean delay across the signal's frequency components, and the group delay variation, which denotes the extent of fluctuation around this average. Group delay variation is critical in assessing the impact of nonlinear phase shifts on signal integrity, especially in wide-band communication systems.

$$\tau(\omega) = -\frac{d\phi(\omega)}{d\omega} \quad (6.11)$$



(a) The relationship between phase and frequency in the band.

(b) The relationship between group delay and frequency in the band.

Figure 6.20

The Fourier series representation can effectively model the relationship between group delay and frequency, as shown in equation (6.12). Using a Fourier series makes it easier to derive the time-domain impulse response by applying the Fourier inverse

transform. This feature is crucial for analyzing the effect of group delay variations on signal propagation and integrity in time domain.

To simplify the computation, the model only uses the first-order term of the Fourier series to describe group delay, as described by equation (6.13). Fig. 6.21 illustrates this simplified model. Using equation (6.13), the phase can be easily calculated, as shown in equation (6.14) and its corresponding transfer function  $H(f) = e^{i\phi(f)}$ .

$$\tau(f) = a_0 + a_1 \cos\left(\frac{2\pi f}{BW}\right) + b_1 \sin\left(\frac{2\pi f}{BW}\right) + \dots + a_i \cos\left(\frac{2i\pi f}{BW}\right) + b_i \sin\left(\frac{2i\pi f}{BW}\right) + \dots \quad (6.12)$$

$$\tau(f) = \frac{\tau_{PP}}{2} \sin\left(\frac{2\pi f}{BW} + \phi_0\right) (\phi_0 = \pi/2) \quad (6.13)$$

$$\phi(f) = \frac{\tau_{PP}}{2} BW \cos\left(\frac{2\pi f}{BW} + \phi_0\right) (\phi_0 = \pi/2) \quad (6.14)$$

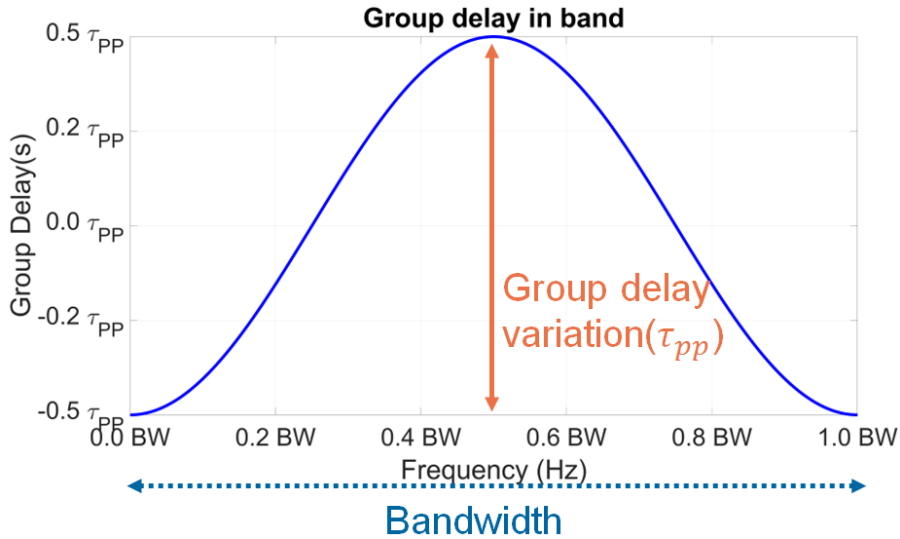


Figure 6.21: The simplest group delay variation model.

After obtaining the transfer function  $H(f)$  for group delay, it is possible to calculate the impact of group delay on the signal. Assuming that the original signal is represented by  $g(t)$  and its frequency expression is denoted by  $G(f)$ . To begin with, calculate the signal in the frequency domain after passing through the group delay model, as shown in equation (6.15). Once this is done, apply the Fourier inverse transform to equation (6.15) to obtain the signal expression in the time domain after being affected by the group delay model. The resulting expression is equation (6.16).

Based on equation (6.16), it becomes apparent that a signal  $\hat{g}(t)$  influenced by group delay splits into two segments. The first segment remains as  $g(t)$ , representing the unaltered original signal that serves as a reference for output. The subsequent segment, defined following the plus sign in the equation, constitutes the error component. This component is responsible for inducing distortion in the signal. Moreover, the magnitude of this error part is determined by the product of the group delay variation  $\tau_{pp}$  and the bandwidth of the signal. This relationship emphasizes the importance of quantifying group delay variation  $\tau_{pp}$  and bandwidth to reduce signal distortion.

$$\hat{G}(f) = G(f)H(f) \quad (6.15)$$

$$\hat{g}(t) \approx g(t) + \frac{\tau_{pp}BW}{4} \cdot \left\{ g\left(t + \frac{1}{BW}\right) \exp\left[j\left(\frac{\pi}{2} + \phi_0\right)\right] + g\left(t - \frac{1}{BW}\right) \exp\left[j\left(\frac{\pi}{2} - \phi_0\right)\right] \right\} \quad (6.16)$$

The time-domain simulation outcomes, illustrating the effects of group delay variation on signal, are depicted in Fig. 6.22. From these results, it is evident that group delay variation significantly alters the output signal, denoted as  $\hat{g}(t)$ , in comparison to the reference signal, referred to as  $g(t)$ . This alteration manifests as distortions in both the amplitude and phase of the signal.

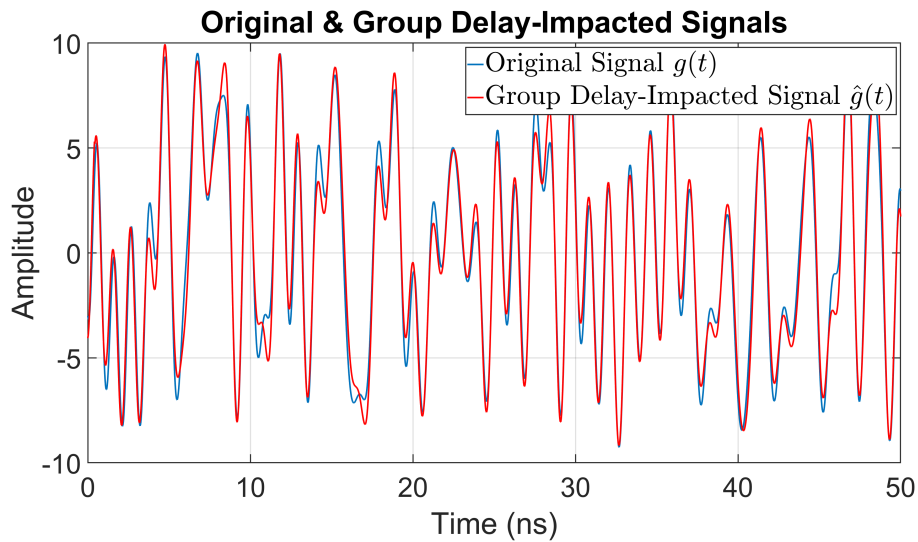


Figure 6.22: Simulation of group delay variation in the time domain.

The presence of group delay variation not only results in distortion of signals in time domain but also adversely affects the EVM of the signal. To clarify the correlation between EVM and group delay variation, consider a basic modulation example, such as a 4-QAM signal, illustrated in Fig. 6.23. By integrating equation (6.16) into equation (6.1) within the context of 4-QAM, it's possible to derive the relationship between EVM and group delay variation as depicted in equation (6.17). This derived relationship reveals that EVM increases in direct proportion to the product of group delay variation ( $\tau_{pp}$ ) and the signal's bandwidth ( $BW$ ). Consequently, minimizing group delay variation is paramount for maintaining low EVM levels, particularly when adhering to specific bandwidth constraints.

$$EVM = \frac{\sqrt{2}}{4} \tau_{pp} BW \quad (6.17)$$

Equation (6.17) lacks variables associated directly with modulation order, suggesting that EVM is unaffected by it. This notion is corroborated by the simulation outcomes presented in Fig. 6.24a, where the modulation order ranges from 4-QAM to 1024-QAM on the x-axis, and EVM is measured in dB on the y-axis. With the simulation parameters set to a constant group delay variation ( $\tau_{pp}$ ) of 15 ps and bandwidth ( $BW$ ) of 2 GHz,

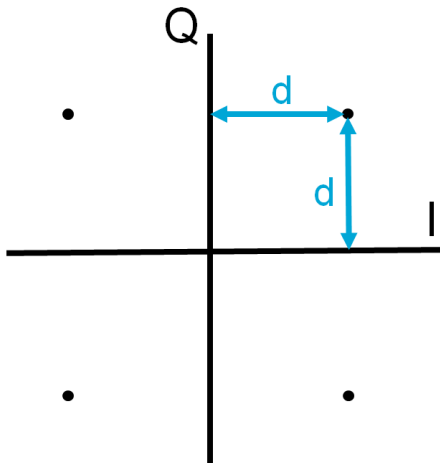


Figure 6.23: The constellation diagram of 4-QAM signal.

the results reveal a critical insight: variations in the modulation order do not substantially affect the EVM. This finding underscores the conclusion that, within the confines of these simulation parameters, EVM's sensitivity to modulation order is minimal. Fig. 6.24b illustrates the relationship between  $\tau_{pp} \times BW$  and EVM, where the x-axis represents the product of  $\tau_{pp}$  and  $BW$ , varying from near 0 to 0.9, and the y-axis displays EVM values in dB. The graph depicts a gradual decline in EVM as  $\tau_{pp} \times BW$  increases. Additionally, the red computational results, which were obtained using equation (6.17) and matched with the simulation results, confirm the direct relationship between the increase in  $\tau_{pp} \times BW$  and the worsening of EVM.

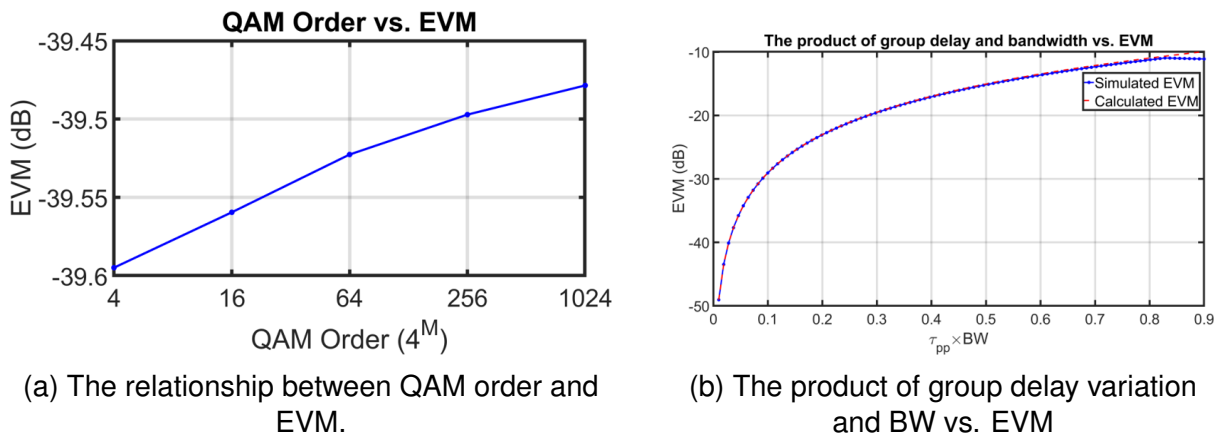


Figure 6.24

For the analysis and simulation of group delay variation, the following important conclusions can be drawn:

1. The product of group delay variation and signal bandwidth is proportional to EVM;
2. To achieve an EVM less than -40 dB, with a BW of 2 GHz, the group delay variation should be less than 15 ps;
3. Considering only group delay, changing the order of QAM does not have a significant impact;

4. The equation is not only applicable to transmitter design but also to estimating the impact of channel group delay.

## 6.4 Other factors deteriorating EVM

Beyond the parameters that influence transmitter performance, external factors can degrade the transmitted signal, requiring consideration. Notably, phase noise from the local oscillator and quantization noise from the digital-to-analog converter (DAC) are significant. The impact of these factors on the Error Vector Magnitude (EVM) is delineated as follows:

1. As shown by equation (6.18),  $EVM_{PN}$  represents the degradation in EVM caused by phase noise. Here,  $\varphi_{RMS}$  denotes the integrated phase noise. When the  $\varphi_{RMS}$  remains below  $0.5^\circ$  degrees, the resulting  $EVM_{PN}$  is calculated to be less than  $-40\text{ dB}$ .

$$EVM_{PN} = \sqrt{\varphi_{RMS}^2} \quad (6.18)$$

2. As shown by equation (6.19),  $EVM_{QN}$  indicates EVM degradation due to quantization noise in DACs, highlighting the precision limitations of digital-to-analog conversion.  $Nb$  is the resolution of the DAC, and  $f_s$  is the DAC's sampling frequency. The resolution of the DAC not only affects the signal's EVM but also, due to the impact of quantization noise, affects the power of the TX leakage signal, especially the leakage signal of transmitter at the Larmor frequency, which may cause deterioration of qubit fidelity. This issue will be analyzed in section 6.6 and 6.7. When the resolution is 8bit and the sampling frequency is  $8\text{ GS/s}$ , the calculated  $EVM_{QN}$  is  $-52\text{ dB}$ .

$$EVM_{QN} = -(6.02Nb + 1.76 + 10 \log 10(f_s/2) + 3.01) + 10 \log 10(BW) + PAPR \quad (6.19)$$

## 6.5 Power Consumption

Furthermore, the analysis extends to power consumption, a critical parameter for transmitters, especially in environments requiring operation at 4K, such as those involving quantum chips. Excessive power dissipation by the transmitter could elevate the ambient temperature around the chip, potentially compromising the integrity and performance of quantum computing components. While the goal is to minimize the total power consumption of the transmitter as much as feasible, it is important to consider that other components of the transceiver, such as the Analog-to-Digital Converter (ADC) and the receiver, also significantly contribute to the overall power consumption. Therefore, the power consumption of the transmitter must be optimized to balance efficiency with the operational requirements of the entire system. Furthermore, the transmission power of the transmitter is approximately 1 mW, and the system efficiency of the transmitter typically falls below 10%. Consequently, estimating the power consumption of the transmitter at 20 mW constitutes a reasonable approximation.

Regarding the power consumption criteria for the entire transceiver, which is stipulated to be below  $100\text{ mW}$  from the QUADRATURE project proposal, the system encompasses the transmitter, receiver, and analog-to-digital converter (ADC), among other circuit components. The distribution of DC power consumption within the transceiver is allocated as follows: approximately 53.2% for the transmitter (TX), 12.7% for the receiver (RX), 34.1% for the local oscillator (LO) [32]. This allocation translates to power consumption figures of  $47.8\text{ mW}$  for the TX,  $11.5\text{ mW}$  for the RX,  $30.7\text{ mW}$  for the LO, and  $10\text{ mW}$  for ADC in alignment with the transceiver's overall power consumption limits. Given the transmitter's power consumption is estimated at  $20\text{ mW}$ , based on its output power and efficiency, there remains a margin within the system's power budget.

## 6.6 Spectrum Mask

The RF signal leakage should not significantly degrade the fidelity of the qubits. Given that the operating frequency of the qubits differs by more than  $10\text{ GHz}$  from that of classical wireless RF transceivers, it is essential to maintain this separation to avoid interference. With RF transceivers operating at  $28\text{ GHz}$  and qubits at the Larmor frequency of  $12\text{ GHz}$ , along with a Rabi frequency of  $10\text{ MHz}$ , the TX leakage within the range of  $12\text{ GHz} \pm 10\text{ MHz}$  must adhere to the results calculated by Chapter 3. Ultimately, in the range of  $12\text{ GHz} \pm 10\text{ MHz}$ , the power spectral density of the transmitted signal leaking into the qubit cavity should be less than  $-140\text{ dBm/Hz}$ , shown as in Fig. 3.7, reflecting these considerations to ensure that the qubits operate correctly without interference from the transceiver's signals. Additionally, the spur of the TX output signal should be less than  $-84\text{ dBm}$  in power at the  $12\text{GHz}$  Larmor frequency. However, there are no restrictions on the power of the transmitted signal in other frequency.

## 6.7 The resolution of DAC

Considering the finite resolution of a digital-to-analog converter (DAC), there exists a deviation between the output signal and the ideal signal. This deviation is known as the quantization error. The relationship between the signal-to-quantization-noise ratio ( $SN_QR$ ) and the DAC's resolution of  $N$  bits is described by the following equation:

$$SN_QR(BW) = 1.76 + 6.02 \times N + 10^{10} \log \left( \frac{f_s/2}{BW} \right) \quad (6.20)$$

With an 8-bit resolution and a  $8\text{ GS/s}$  sampling rate for the Digital-to-Analog Converter (DAC), and a signal bandwidth of  $2\text{ GHz}$ , application of these parameters to equation (6.20) yields a Signal-to-Noise-and-Quantization Ratio ( $SN_QR$ ) of  $53\text{ dB}$ . Given the transmitter's output power of  $-1\text{ dBm}$ , we can deduce the quantization noise to be  $-54\text{ dBm}$ , utilizing the equation  $P_{QN} = P_{TX} - SN_QR$ . With a  $8\text{ GS/s}$  sampling frequency, this results in a quantization noise power spectral density (PSD) of  $-153\text{ dBm/Hz}$ . Ultimately, in assessing the PSD of the DAC's quantization noise against the spectral requirements, the  $kT$  noise spectrum, as depicted in Fig. 6.25, indicates that a DAC with an 8-bit resolution and a  $8\text{ GS/s}$  sampling rate sufficiently meets the specifications for the transmitted signal's spectrum.

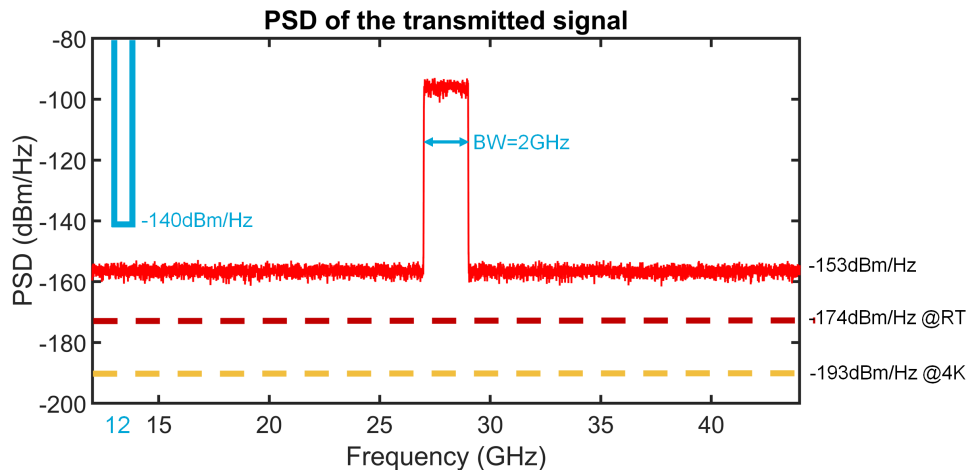


Figure 6.25: The PSD of a transmitted signal.

## 6.8 Conclusion

Given that the elements affecting EVM operate independently, the transmitter's overall EVM can be derived using equation (6.2). To achieve an overarching goal of having an EVM of less than -32 dB, it is necessary to break down the EVM into specific component requirements, as depicted in Table 6.1. Following this breakdown, Table 6.2 outlines the essential specifications for the transmitter design to meet these EVM criteria. This defines the design requirements for the transmitter.

Table 6.1: EVM Requirements

<b>EVM Requirements</b>	
$EVM_{QN}$	$\leq -50 \text{ dB}$
$EVM_{PN}$	$\leq -40 \text{ dB}$
$EVM_{IQMis}$	$\leq -40 \text{ dB}$
$EVM_{LOFT}$	$\leq -40 \text{ dB}$
$EVM_{PA}$	$\leq -40 \text{ dB}$
$EVM_{GDV}$	$\leq -40 \text{ dB}$

Table 6.2: Transmitter Design Specifications

<b>Transmitter Design Requirements</b>	
DAC resolution	$\geq 8 \text{ bit}$
$\varphi_{\text{RMS}}$	$\leq 0.5^\circ$
Phase Mismatch	$\leq 1^\circ$
Amplitude Mismatch	$\leq 0.2 \text{ dB}$
LO Feedthrough Leakage	$\leq -40 \text{ dBc}$
OP1dB	$\geq 12 \text{ dBm}$
$\Phi_{\max}$	$\leq 1^\circ$
Group Delay Variation ( $\tau_{pp}$ )	$\leq 15 \text{ ps}$
Power Consumption	$\leq 20 \text{ mW}$

## 7. Mapping the specifications on the receiver design

### 7.1 Introduction

In this chapter, we will discuss the receiver design. Referring to 5GHz wireless transfer, noise figure becomes a critical specification to characterize the performance of this receiver. However, unlike this application, we care more about power since this receiver operates at cryo-temperature. Additionally, LNA determines the noise of the receiver and contributes to most of the power. So, we firstly analyze the LNA taped-out last year in Sec. 7.2 and the specification improvement of this LNA in the next version in Sec. 7.3, especially the trade-off between power and noise in Sec. 7.4. Then, the lock-in receiver taped-out last year is proposed in Sec. 7.5. Specifications of the improved polar receiver are defined in Sec. 7.6. In Sec. 7.7 and 7.8, we distribute the power consumption of the receiver and outline the specifications.

### 7.2 Overview of cryogenic LNA

We have developed and measured a compact cryo-LNA operating up to 8.8 GHz representing the initial version of a component within this receiver. Our cryo-LNA is implemented in SiGe BiCMOS process, known for its versatility in enabling the design of both digital/analog mixed-signal building blocks and low-noise RF building blocks employing SiGe heterojunction bipolar transistors (HBTs). Additionally, HBTs exhibit significantly lower 1/f noise compared to field-effect transistors (FETs).

This design is a variant of the conventional Meyer topology [29]. A single shunt feedback is applied to scale down the input impedance by around a factor of the loop gain so as to achieve wideband impedance matching. We use the cascode structures as the primary amplification core in our design for robust stability and enhance single-stage gain.

Based on the measurement results, the LNA achieves an average noise temperature of 5K across the frequency range of 0.1-6 GHz with a VDD of 1.7 V. Additional measurement results will be presented in the table.

### 7.3 Improvement for LNA

For the wireless communication between cores, we select a carrier frequency of 28 GHz as discussed in Sec. 5.1. To accommodate this frequency range and extrapolate the bandwidth from 8.8 GHz to 28 GHz for our system, we plan to implement dou-

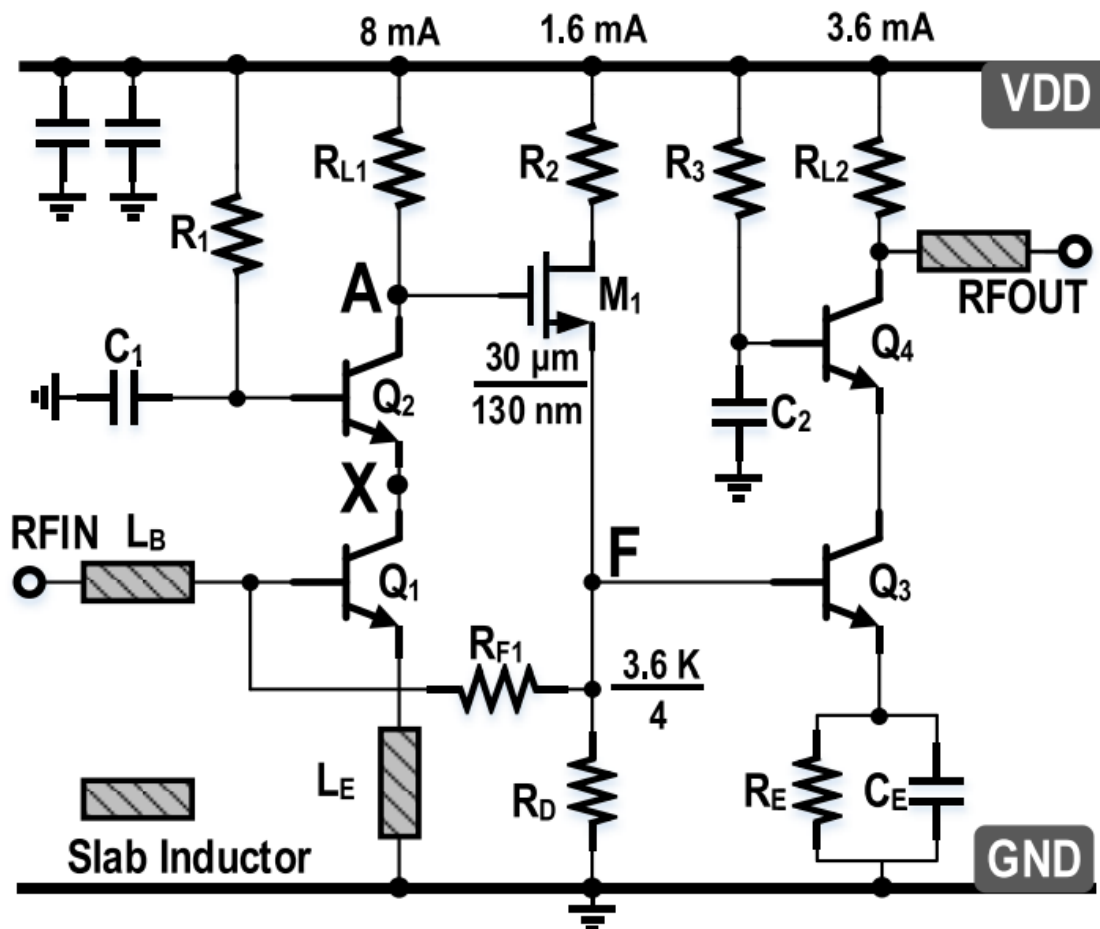


Figure 7.1: Topology of the BiCMOS wideband low-noise amplifier

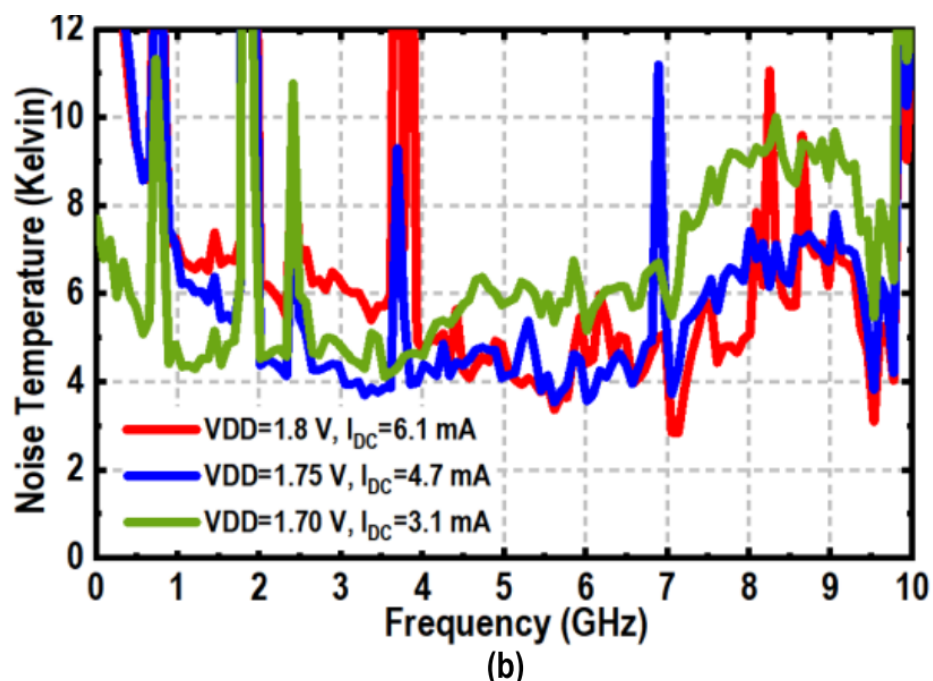


Figure 7.2: Measured noise temperature of the LNA

<b>Technology</b>	130nm SiGe BiCMOS
<b>Gain</b>	33-36 dB
<b>Frequency Range</b>	0.1-8.8 GHz
<b>Noise Temperature</b>	4-10.5 K
<b>Power Consumption</b>	8.2 mW

Table 7.1: Specifications of the existing LNA

ble capacitive zero peaking structures in the LNA. This strategy aims to broaden the bandwidth effectively, ensuring efficient transmission.

Furthermore, during the design of this LNA, it's feasible to achieve a noise figure as low as 0.06 dB (4 K noise temperature) at the expense of increased power consumption. However, considering the acceptable noise figure according to the link budget analysis (< 5 dB), there is still room for careful optimization of power consumption of this LNA.

The simulated static current of every stage in LNA and the total LNA current consumption at CT are highlighted in Fig.7.3. With a significant increase in transconductance by approximately five times at CT, the current consumption of the first and second stages could be effectively reduced from 8 to 2.8 mA and from 3.6 to 1.5 mA, respectively. Accordingly, noise figure will be increased. So the tradeoff between noise figure and power will be discussed in next section.

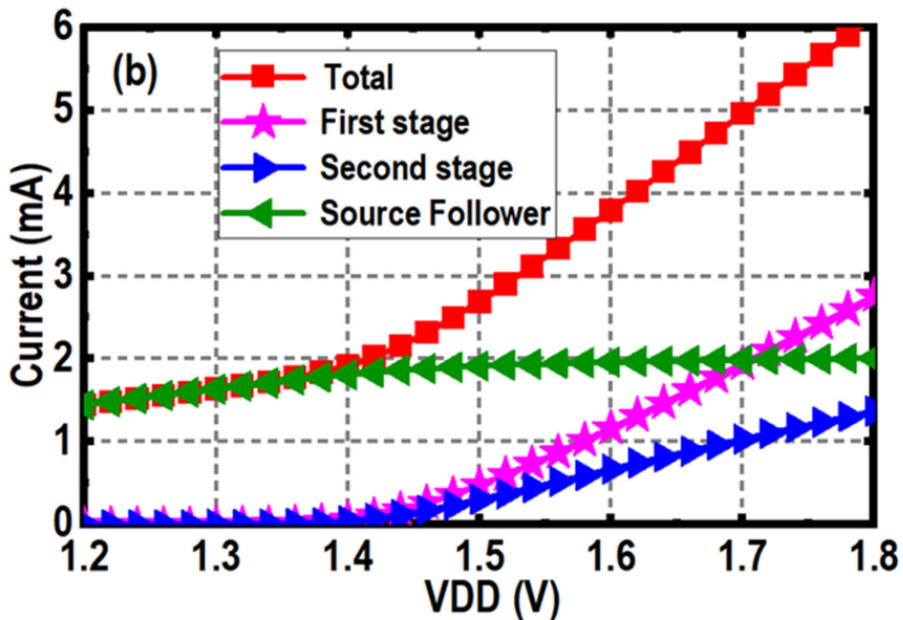


Figure 7.3: Anticipated statics of the current variation versus the supply voltage using the cryogenic static models.

## 7.4 Noise and power trade-off for LNA

The noise temperature or noise figure have become the standard figures of merit for low noise systems. The importance of gain in terms of system noise temperature can be understood by considering Friss's formula [12]:

$$T_{RX} = T_{e1} + \frac{T_{e2}}{G_{a1}} + \frac{T_{e3}}{G_{a1}G_{a1}} + \dots \quad (7.1)$$

where  $T_{RX}$  is the overall input referred noise temperature,  $T_{e1}$  and  $G_{a1}$  are the noise temperature and available gain of the LNA,  $T_{e2}$  and  $G_{a1}$  are the noise temperature and available gain of the second amplification stage, and so on. The overall input-referred noise temperature of the receiver is primarily contributed by the first stage, the LNA. If the gain of the LNA is set to be approximately 20-40 dB, then the noise temperature of other parts becomes negligible. The noise-temperature of LNA can be described by the formula [17],

$$T_{CAS} = \frac{T_{\min} + T_0 \frac{R_n}{\Re\{Y_{OPT}\}\Re\{Y_S\}} |Y_S - Y_{OPT}|^2}{1 - \frac{1}{G_{a,\max}} - \frac{\Re\{Y_{22}\}}{\Re\{Y_S\}|Y_{21}|^2} |Y_S - Y_{OPT,G}|^2} \quad (7.2)$$

where  $G_{a,\max}$  is the maximum available gain of the LNA. It should be noticed here that noise matching is desired by ensuring the input admittance  $Y_s$  equal to an optimal admittance  $Y_{OPT}$ . However, in gain matching conditions where maximum power transfer is achieved, the input admittance should match an input value  $Y_{s,gain} = \frac{1}{Z_0}$ , where  $Z_0$  is commonly set to 50 Ω to match conventional high-frequency cables. It is advantageous for a design to have overlapping  $Y_{OPT}$  and  $Y_{s,gain}$ . Otherwise, it is desirable to have a small noise resistor  $R_n$  when intentionally terminating the source at a value different from  $Y_{OPT}$ . From the noisy two-port linear theory,  $R_n$  can be expressed as:

$$R_n = r_b + \frac{kT}{2qI_c} \quad (7.3)$$

We accomplished DC and RF characterization of HBT from cryo temperature to room temperature. From one aspect, It can be seen that the  $r_b$  is inversely proportional to current, indicating that part of this noise is strongly inversely related to the trend of power consumption.

From another aspect, the relationship between  $T_{\min}$  and current is more complex in Fig.7.5. However, our focus lies on the current density exceeding 0.01 mA/μm<sup>2</sup>, where the bandwidth can achieve approximately gigahertz. Within the range of 0.01-1 mA/μm<sup>2</sup>, the noise temperature can remain at a low value. Subsequently, with higher power consumption, the noise temperature will be enhanced dramatically, which is a scenario we aim to avoid.

Extrapolating to 28 GHz LNA, if the bandwidth can be tuned by the zeros combined by load capacitance,  $T_{\min}$  will be less sensitive to the frequency if biased more than 0.1 mA/μm<sup>2</sup> shown in in Fig.7.6.

Therefore, considering factors such as noise resistance, minimum noise temperature, and frequency sensitivity, a better trade-off will be achieved if the current density can be controlled between 0.1 – 10 mA/μm<sup>2</sup>. Optimal noise performance can be attained with higher power consumption if the current density is below 0.1 mA/μm<sup>2</sup>. Within the range of 0.1 – 10 mA/μm<sup>2</sup>, the minimum noise temperature  $T_{\min}$  will not be

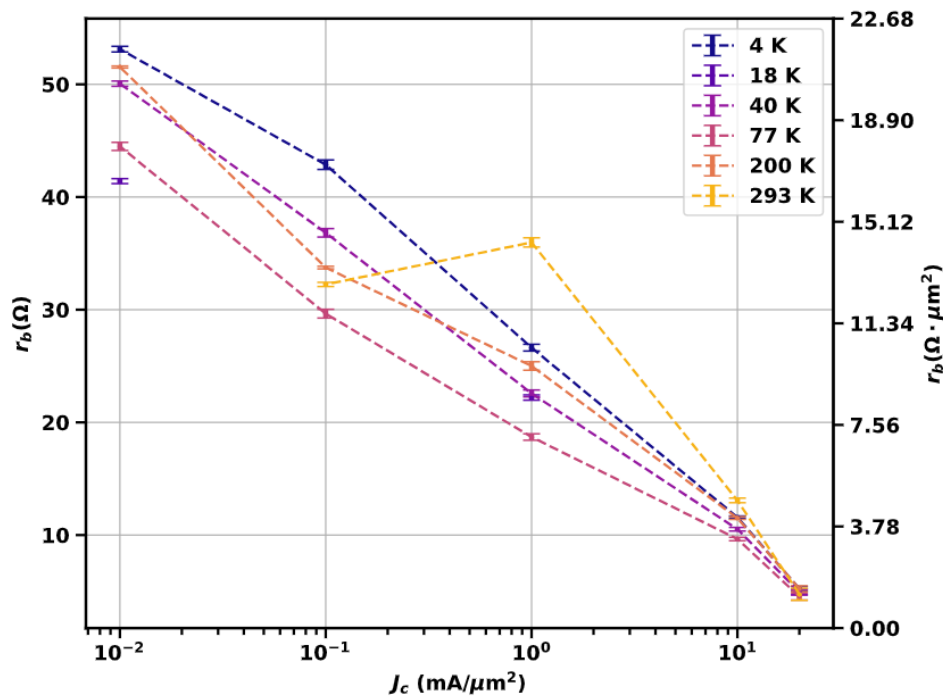


Figure 7.4: Base resistance  $r_b$  as a function of collector current densities

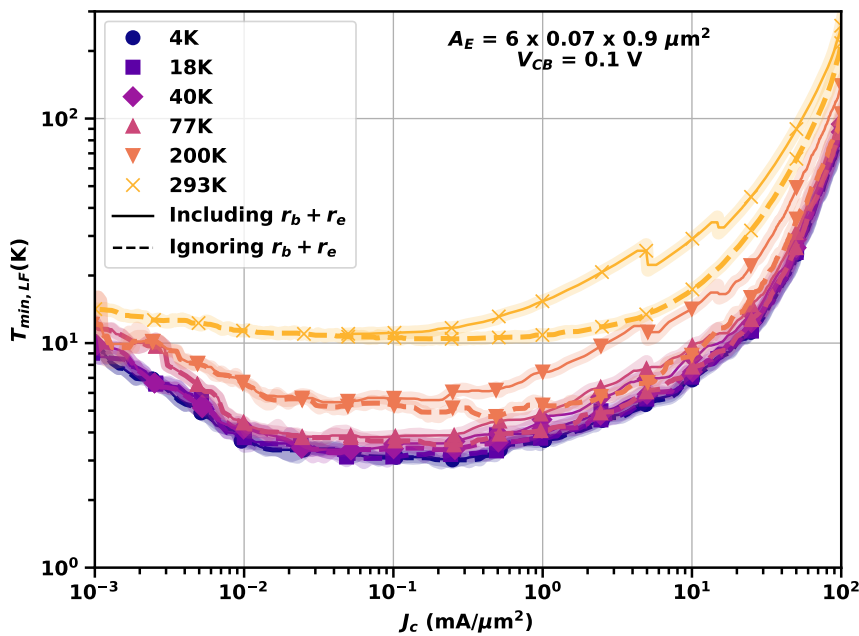


Figure 7.5: Minimum noise temperature  $T_{min}$  as a function of collector current densities

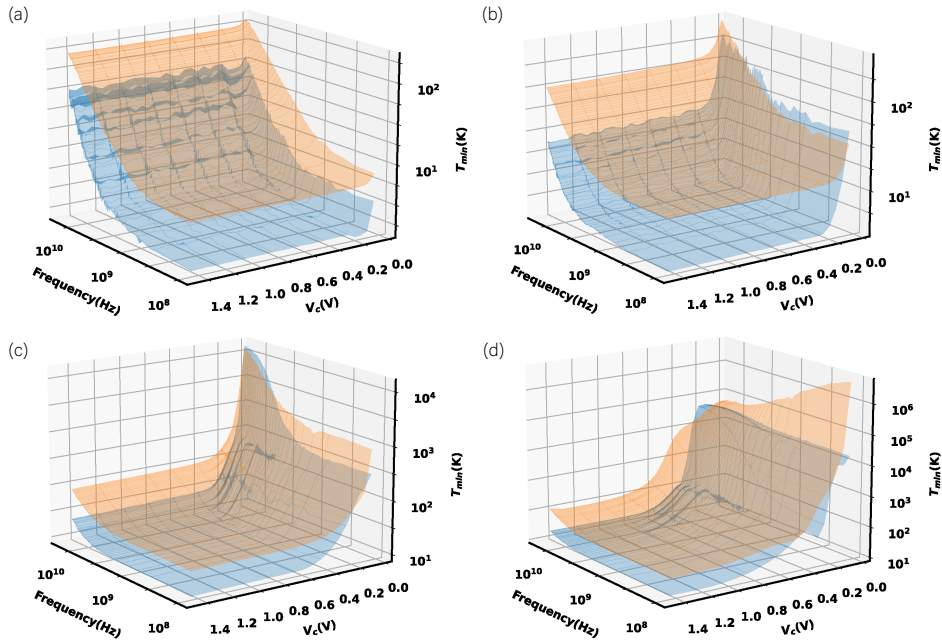


Figure 7.6: Minimum noise temperature ( $T_{min}$ ) as a function of both the frequency for four different current densities: (a)  $J_c = 0.01 \text{ mA}/\mu\text{m}^2$ , (b)  $J_c = 0.1 \text{ mA}/\mu\text{m}^2$ , (c)  $J_c = 1 \text{ mA}/\mu\text{m}^2$ , and (d)  $J_c = 20 \text{ mA}/\mu\text{m}^2$ .

significantly affected, allowing for a wide frequency band and optimized minimum noise temperature. However, if the current density exceeds  $10 \text{ mA}/\mu\text{m}^2$ , although the noise resistance may decrease, the minimum noise temperature will be further enhanced, indicating a less favorable trade-off.

## 7.5 Overview of cryogenic receiver

In Dec. 2023, we completed the tape-out of a lock-in receiver operating up to 8 GHz, which can be seen as the prototype. Our primary objective in this version was to achieve low power consumption and low noise levels. In the subsequent version, we plan to enhance the operating frequency based on the achievements of this prototype.

Different from traditional mixer, we introduced a current domain passive mixer in this design, which operates without consuming DC power and contributes less flicker noise due to reduced fluctuations in DC biasing. Additionally, we proposed a novel hybrid chopper in the amplification stage to further reduce noise. By Jun. 2024, we expect that the measured noise figure will be less than 0.2 dB, and the power consumption will be below 20 mW.

## 7.6 Improvement for receiver

Given the limitation of the lock-in receiver to meet the higher frequency requirement of 28 GHz while maintaining low power consumption, we are exploring an alternative solution. Our proposal involves designing a cryo-polar receiver, which can alleviate the power burden associated with rebuilding the signal. In this approach, the time-to-

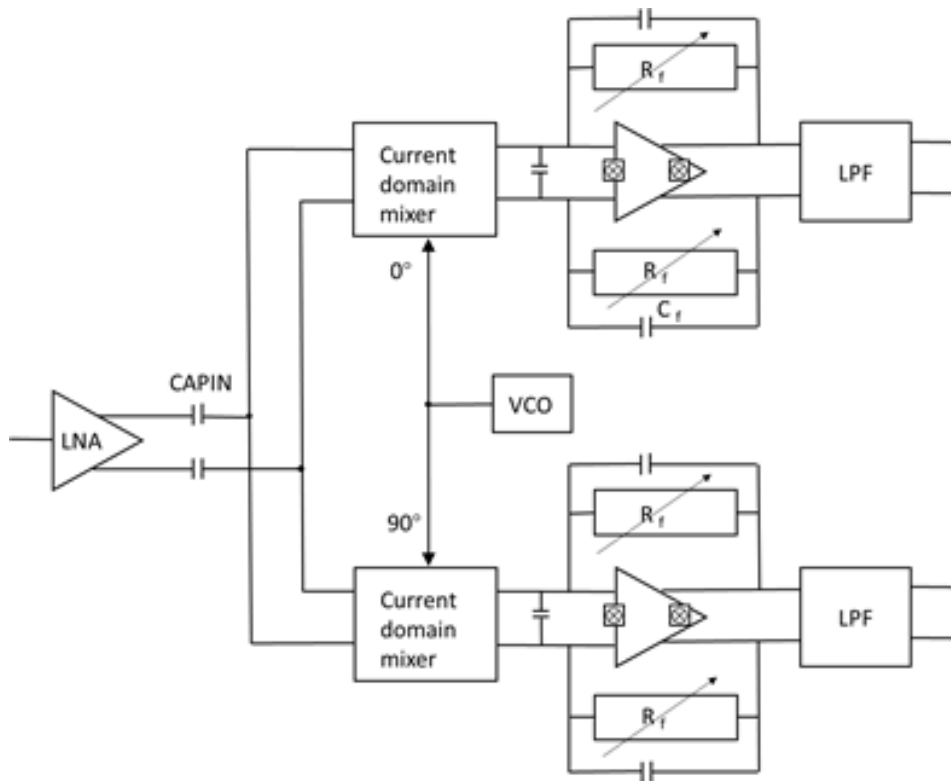


Figure 7.7: Architecture of the lockin receiver

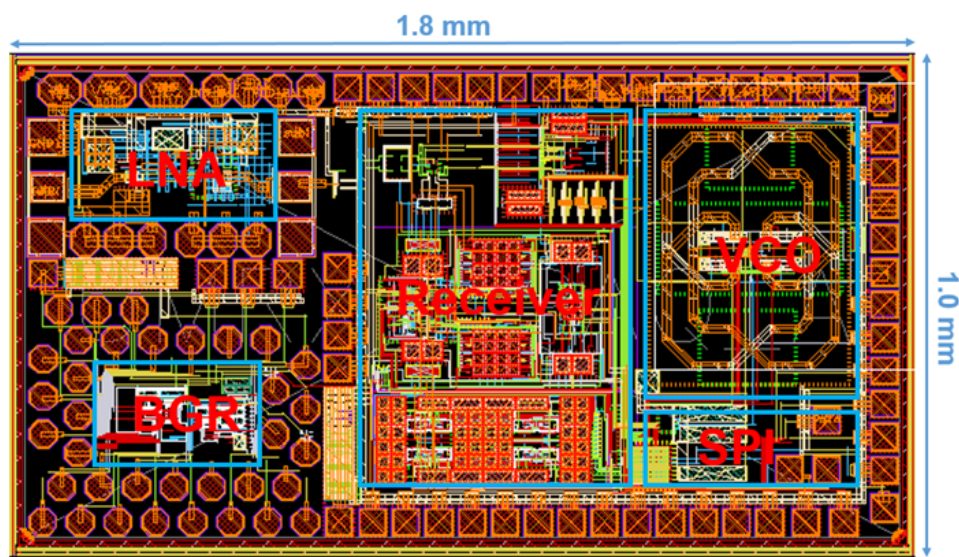


Figure 7.8: Micrograph of the lockin receiver, Tech: SiGe BiCMOS IHP 130nm, 1.4 V,  
Date: Tapeout on 15th Dec. 2023, will be measured in Jun. 2024

digital converter (TDC) and analog-to-digital converter (ADC) are employed to detect amplitude and phase information separately. Key components from the initial version tape-out, including the LNA, amplification stage, low-pass filter (LPF), and others, can still be utilized in the cryo-polar receiver. We intend to leverage more advanced technology, such as the 40nm process node, to enhance their performance and power efficiency. In this polar receiver design, we propose an intermediate frequency (IF) downconversion to 18 GHz as the initial step. This approach aims to alleviate the power efficiency burden associated with ultra-high-speed converters. The sampling time of the ADC will be adjusted dynamically according to the zero-point achieved by the time-to-digital converter (TDC), enabling us to optimize power consumption significantly.

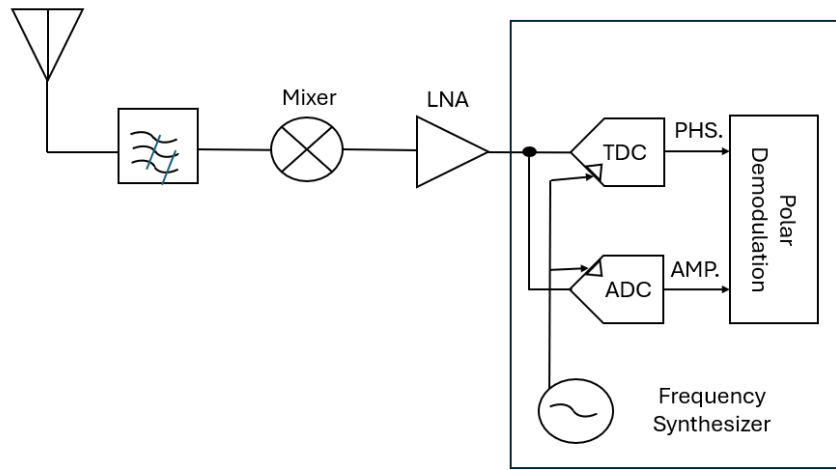


Figure 7.9: Architecture of improved polar receiver

## 7.7 Feasibility

State-of-the-art wireless transceivers are mostly designed for 5G applications at room temperature. Different from these architectures, our transceiver is implemented at cryogenic temperature for quantum applications, which means the power consumption is more important. We have carefully distributed power among different blocks within our transceiver. As discussed above, the LNA operating at 28GHz will achieve a tradeoff at 10-20 mW power consumption and < 5dB noise figure, which will be comparable to the [24] [9] implemented in 28nm and 22nm. We estimate a power consumption of 10mW for VCO [41]. For the TDC part, power budget of 10 mW is allocated according to this polar receiver with carrier frequency at 6 GHz [40].

## 7.8 Conclusion

In this chapter, we discussed about the cryo-polar receiver especially LNA, as the noise performance of this stage significantly impacts the overall resolution of the sys-

Component	Power Consumption (mW)
Total	50
LNA	20
VCO	10
TDC	10
Other Parts (including buffer)	10

Table 7.2: Power Consumption Distribution

Specification	Value
Noise Figure	5 dB
Power Consumption	50 mW
IP1dB	-25 dBm
SFDR	45 dB

Table 7.3: Receiver Performance Specifications

tem. Based on our characterization and measurement results, we have identified that achieving a better trade-off between power consumption and noise performance is possible by setting the current density between  $0.1$  and  $10\text{ mA}/\mu\text{m}^2$  considering the noise resistance, minimum noise temperature, frequency sensitivity. For the receiver, key performance metrics such as noise figure and power consumption have been defined. Additionally, the linearity performance such as 1dB pressing point and SFDR are listed in the table referred to wireless receiver [40].

By carefully managing power distribution and leveraging state-of-the-art technologies, our transceiver aims to achieve a balance between performance and power efficiency, making it well-suited for demanding quantum applications.

# 8. Advanced Transceiver Functionalities

In this chapter, we delve deep into the advanced functionalities of transceivers, specifically focusing on the challenges of delay spread. We begin by introducing Time Reversal (TR) as a potential solution, followed by a comprehensive discussion on its possibilities of implementation on transceivers.

## 8.1 Overview of Time-Reversal

Research has already shown that a primary challenge in Wireless Network-on-Chip (WNoC) lies in mitigating interference and the effects of high delay spread (DS) in reverberant channels to establish multiple parallel high-speed links [7]. Time Reversal (TR), which uses the multipath richness of the channel to overcome the undesired effects of delay spread, becomes a promising new solution.

Time Reversal (TR) is a technique that employs knowledge of the wireless channel impulse response to create an ideal matched filter [23]. In specific, it focuses the received signal energy to its source with back propagation, upon creating a signal reversed in time with prior Channel State Information (CSI). Its advantages in rich scattering environments are well understood and validated through various studies, including the field of acoustics, wireless communications at microwave frequencies [22] and sub-terahertz bands [5, 30]. By combining TR with various modulation schemes, it has the potential to transmit data at speeds faster than those typically allowed by channel delay spreading. [18, 25].

The implementation of Time Reversal (TR) in conventional wireless networks faces challenges due to dynamic channel variations. The need for constantly obtaining the Channel State Information (CSI) and implementing a filter that can adapt to changes in the CSI makes the practical implementation of TR in these environments difficult. However, the unique aspects of the on-chip scenario significantly simplify these challenges.

In our project, the wireless channel, despite its complexity, is deterministic and practically invariant in time. These mean that the geometry, material characteristics, and node locations can be precisely determined in advance and remain unchanged after fabrication and integration. Such information allows accurate pre-modelling of the channel, thereby simplifying compensating for the channel's impairments using various techniques. In other words, the wireless in-package channel is static and can be pre-characterized accurately.

In this context (wireless in-package environment), the essence of TR lies in its application as a match-filter at the transmitter, see Fig.8.1.

This application ensures the radiated signal is focused in time, with a peak much shorter than the length of the impulse response, and in space, around a targeted re-

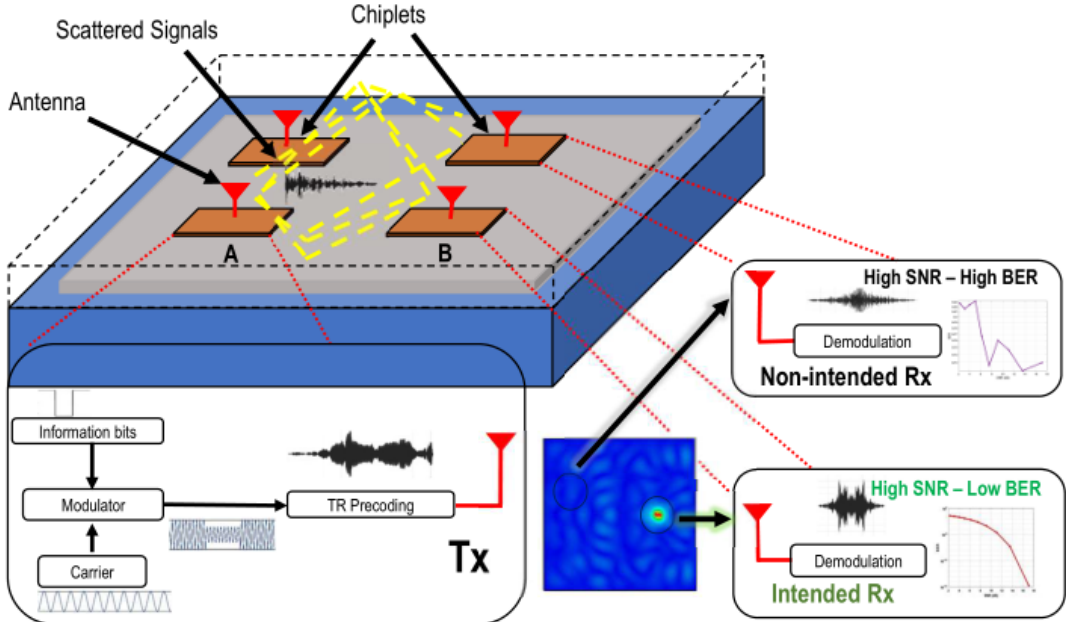


Figure 8.1: Time reversal in a wireless in-package environment [7]

ceiver. This method not only mitigates potential Inter-Symbol Interference (ISI) effects but also compresses undesirable interference on adjacent transceivers. Consequently, it facilitates the creation of multiple parallel spatial channels.

## 8.2 Further Research Direction

In this section, possibilities to implement TR in the transceiver design are explored. In Ref. [7], the TR technique is evaluated with infinite sampling resolution. With a finite sampling speed, the filter can be directly implemented as a Feedforward Equalizer (FFE) in the baseband of the transmitter. Typically, there are two ways to implement FFE, either in the frequency domain or in the time domain. For frequency domain equalizers [37], they are mostly implemented in the digital domain. Such digital implementation usually incurs high power consumption. And digital power efficiency degrades quickly with high data rates, which is not attractive for our application. Compared with the former, time-domain mixed-signal equalizers [10] have been shown to be more energy efficient. However, the potential MIMO complexity with low delay requirements is also challenging. With this approach, the trade-off between coefficient numbers, power, area, and modulation scheme could be explored in the future.

Since the frequency response of the channel is known, the Signal-to-Noise ratio(SNR) can also be enhanced by designing a bandpass filter with an interest frequency band on the receiver side. Therefore, noise-shaping and especially continuous time Delta-Sigma Modulators are very attractive in such a scenario. However, the signal bandwidth of this technique is usually limited(less than 200MHz) [28]. To meet the high-bandwidth requirement in our project, a frequency-interleaving ADC array could be explored [26].

## 9. Conclusions

To achieve a larger processing power, QUADRATURE envisions connecting several smaller quantum processors by both classical and quantum links. This report describes the requirements of such a wireless communication link to achieve entanglement among different quantum cores. In Chapter 2, the data rate of the classical wireless link is estimated by analyzing the number of entangling operations between the cores and posing a limit on the latency of the data exchange due to the limited qubit coherence. It was concluded that a data rate of 12 Gbps would be enough to support an 8-core processor with 99.9% fidelity. In Chapter 3, the operating frequency of the classical link is chosen 28GHz by considering the effect of undesired emission of the classical transmitter on the fidelity of the quantum link, the power efficiency of the power amplifiers, transceiver power consumption, antenna size, and practical limitations of the available measurement setups. By employing the developed electromagnetic model of the wireless channel and using the link budget equations, Chapter 5 estimated the required high-level specifications of the transceiver, e.g., a signal bandwidth of 2 GHz with 64-QAM modulation scheme, a transmitting output power of -1 dBm and a receiver noise figure of 5 dB. Chapters 6 and 7, respectively, discussed in detail the required specification of the transmitter and receiver in terms of the resolution of amplitude needed for digital-to-analog converters, in-phase and quadrature mismatch, output and input 1-dB compression points and group delay of the matching networks and filters. Chapter 8 proposed employing the time reversal technique to alleviate the large delay spread and small coherent bandwidth of the wireless channel imposed by the small and reflective package of the quantum processor. By knowing all system- and block-level specifications of the classical wireless link presented in this report, WP2 can start the transceiver's circuit design without any delay.

# Bibliography

- [1] Study on new radio (nr) to support non-terrestrial networks (release 15). Technical Report TR 38.815 V15.1.0, 3rd Generation Partnership Project (3GPP), Sept. 2021. URL: <https://portal.3gpp.org/desktopmodules/Specifications/SpecificationDetails.aspx?specificationId=3298>.
- [2] CST Microwave Studio, 2022.
- [3] S. Abadal, C. Han, and J. M. Jornet. Wave propagation and channel modeling in chip-scale wireless communications: A survey from millimeter-wave to terahertz and optics. *IEEE access*, 8:278–293, 2019.
- [4] E. Alarcón, S. Abadal, F. Sebastianiano, M. Babaie, E. Charbon, P. H. Bolívar, M. Palesi, E. Blokhina, D. Leipold, B. Staszewski, A. Garcia-Sáez, and C. G. Almudever. Scalable multi-chip quantum architectures enabled by cryogenic hybrid wireless/quantum-coherent network-in-package. In *2023 IEEE International Symposium on Circuits and Systems (ISCAS)*, pages 1–5, 2023.
- [5] G. C. Alexandropoulos, A. Mokh, R. Khayatzadeh, J. De Rosny, M. Kamoun, A. Ourir, A. Tourin, M. Fink, and M. Debbah. Time reversal for 6g spatiotemporal focusing: Recent experiments, opportunities, and challenges. *IEEE Vehicular Technology Magazine*, 2022.
- [6] L. Anttila, M. Valkama, and M. Renfors. Frequency-selective i/q mismatch calibration of wideband direct-conversion transmitters. *IEEE Transactions on Circuits and Systems II: Express Briefs*, 55(4):359–363, 2008.
- [7] A. Bandara, F. Rodríguez-Galán, E. P. de Santana, P. H. Bolívar, E. Alarcón, and S. Abadal. Exploration of time reversal for wireless communications within computing packages. In *Proceedings of the 10th ACM International Conference on Nanoscale Computing and Communication*, pages 14–20, 2023.
- [8] E. T. Campbell, B. M. Terhal, and C. Vuillot. Roads towards fault-tolerant universal quantum computation. *Nature*, 549(7671):172–179, 2017.
- [9] B. Cui and J. R. Long. A 1.7-db minimum nf, 22–32-ghz low-noise feedback amplifier with multi-stage noise matching in 22-nm fd-soi cmos. *IEEE Journal of Solid-State Circuits*, 55(5):1239–1248, 2020.
- [10] K. Dasgupta, S. Daneshgar, C. Thakkar, S. Kang, A. Chakrabarti, S. Yamada, N. Narevsky, D. Choudhury, J. E. Jaussi, and B. Casper. A 60-ghz transceiver and baseband with polarization mimo in 28-nm cmos. *IEEE Journal of Solid-State Circuits*, 53(12):3613–3627, 2018.
- [11] P. Escofet, A. Ovide, C. G. Almudever, E. Alarcon, and S. Abadal. Hungarian qubit assignment for optimized mapping of quantum circuits on multi-core architectures. *IEEE Computer Architecture Letters*, 22(02):161–164, jul 2023.
- [12] H. T. Friis. Noise figures of radio receivers. *Proceedings of the IRE*, 32(7):419–422, 1944.
- [13] E. Genender, C. L. Holloway, K. A. Remley, J. M. Ladbury, G. Koepke, and H. Garbe. Simulating the multipath channel with a reverberation chamber: Application to bit error rate measurements. *IEEE Transactions on Electromagnetic Compatibility*, 52(4):766–777, 2010.
- [14] D. Gottesman and I. L. Chuang. Demonstrating the viability of universal quantum computation using teleportation and single-qubit operations. *Nature*, 402:390–393, 11 1999.
- [15] A. Grami. *Introduction to digital communications*. Academic Press, 2015.

- [16] T. Green, H. Uys, and M. J. Biercuk. High-order noise filtering in nontrivial quantum logic gates. *Physical review letters*, 109(2):020501, 2012.
- [17] H. Haus, W. Atkinson, G. Branch, W. Davenport, W. Fonger, W. Harris, S. Harrison, W. McLeod, E. Stodola, and T. Talpey. Representation of noise in linear twoports. *Proceedings of the IRE*, 48(1):69–74, 1960.
- [18] Y. Jin, D. Zhao, and Y. Ying. Time reversal data communications on pipes using guided elastic waves: Part i. basic principles. In *Health Monitoring of Structural and Biological Systems 2011*, volume 7984, pages 92–103. SPIE, 2011.
- [19] E. Kawakami, P. Scarlino, D. R. Ward, F. Braakman, D. Savage, M. Lagally, M. Friesen, S. N. Coppersmith, M. A. Eriksson, and L. Vandersypen. Electrical control of a long-lived spin qubit in a si/sige quantum dot. *Nature nanotechnology*, 9(9):666–670, 2014.
- [20] H.-T. Kim, B.-S. Park, S.-S. Song, T.-S. Moon, S.-H. Kim, J.-M. Kim, J.-Y. Chang, and Y.-C. Ho. A 28-ghz cmos direct conversion transceiver with packaged  $2 \times 4$  antenna array for 5g cellular system. *IEEE Journal of Solid-State Circuits*, 53(5):1245–1259, 2018.
- [21] S. Laha, S. Kaya, D. W. Matolak, W. Rayess, D. DiTomaso, and A. Kodi. A new frontier in ultralow power wireless links: Network-on-chip and chip-to-chip interconnects. *IEEE Transactions on Computer-Aided Design of Integrated Circuits and Systems*, 34(2):186–198, 2015.
- [22] G. Lerosey, J. De Rosny, A. Tourin, A. Derode, G. Montaldo, and M. Fink. Time reversal of electromagnetic waves. *Physical review letters*, 92(19):193904, 2004.
- [23] G. Lerosey, J. De Rosny, A. Tourin, A. Derode, G. Montaldo, and M. Fink. Time reversal of electromagnetic waves and telecommunication. *Radio science*, 40(06):1–10, 2005.
- [24] H.-T. Lin, L. Gao, H.-Y. Li, J.-X. Xu, and X. Y. Zhang. A 23.6–46.5 ghz lna with 3 db nf and 24 db gain tuning range in 28-nm cmos technology. *IEEE Transactions on Circuits and Systems I: Regular Papers*, 2023.
- [25] S. Liu, Z. Zhao, R. Chen, and W. Wu. Time reversal pulse position modulation communication in shallow water acoustic channels. *Applied Acoustics*, 182:108249, 2021.
- [26] R. Lu and M. P. Flynn. A direct frequency-interleaving continuous-time bandpass delta-sigma adc. *IEEE Transactions on Circuits and Systems I: Regular Papers*, 2023.
- [27] O. Markish, B. Sheinman, O. Katz, D. Corcos, and D. Elad. On-chip mmWave Antennas and Transceivers. In *Proceedings of the NoCS ’15*, page Art. 11, 2015.
- [28] D. J. McLaurin, K. G. Gard, R. P. Schubert, M. J. Mangani, H. Zhu, D. Alldred, Z. Li, S. R. Bal, J. Fan, O. E. Gysel, et al. A highly reconfigurable 65nm cmos rf-to-bits transceiver for full-band multicarrier tdd/fdd 2g/3g/4g/5g macro basestations. In *2018 IEEE International Solid-State Circuits Conference-(ISSCC)*, pages 162–164. IEEE, 2018.
- [29] R. Meyer, R. Eschenbach, and R. Chin. A wide-band ultralinear amplifier from 3 to 300 mhz. *IEEE Journal of Solid-State Circuits*, 9(4):167–175, 1974.
- [30] A. Mokh, J. de Rosny, G. C. Alexandropoulos, M. Kamoun, A. Ourir, R. Khayatzadeh, A. Tourin, and M. Fink. Experimental validation of time reversal multiple access for uwb wireless communications centered at the 273 ghz frequency. In *2022 IEEE 95th Vehicular Technology Conference:(VTC2022-Spring)*, pages 1–5. IEEE, 2022.
- [31] J. T. Muhonen, J. P. Dehollain, A. Laucht, F. E. Hudson, R. Kalra, T. Sekiguchi, K. M. Itoh, D. N. Jamieson, J. C. Mccallum, A. S. Dzurak, and A. Morello. Storing quantum information for 30 seconds in a nanoelectronic device. *Nature Nanotechnology*, 9(12):986–91, 12 2014.
- [32] J. Pang, R. Wu, Y. Wang, M. Dome, H. Kato, H. Huang, A. Tharayil Narayanan, H. Liu, B. Liu, T. Nakamura, T. Fujimura, M. Kawabuchi, R. Kubozoe, T. Miura, D. Matsumoto, Z. Li, N. Oshima, K. Motoi, S. Hori, K. Kunihiro, T. Kaneko, A. Shirane, and K. Okada. A 28-ghz cmos phased-array transceiver based on lo phase-shifting architecture with gain invariant phase tuning for 5g new radio. *IEEE Journal of Solid-State Circuits*, 54(5):1228–1242, 2019.
- [33] S. G. Philips, M. T. Madzik, S. V. Amitonov, S. L. de Snoo, M. Russ, N. Kalhor, C. Volk, W. I. Lawrie, D. Brousse, L. Tryputen, et al. Universal control of a six-qubit quantum processor in silicon. *Nature*, 609(7929):919–924, 2022.

- [34] B. Prabowo, G. Zheng, M. Mehrpoo, B. Patra, P. Harvey-Collard, J. Dijkema, A. Sammak, G. Scappucci, E. Charbon, F. Sebastiano, L. M. K. Vandersypen, and M. Babaie. 13.3 a 6-to-8ghz 0.17mw/qubit cryo-cmos receiver for multiple spin qubit readout in 40nm cmos technology. In *2021 IEEE International Solid-State Circuits Conference (ISSCC)*, volume 64, pages 212–214, 2021.
- [35] B. Razavi and R. Behzad. *RF microelectronics*, volume 2. Prentice hall New York, 2012.
- [36] D. Rossi and G. Ansaloni. D3. 3: Adaptive protocol stack.
- [37] N. Saito, T. Tsukizawa, N. Shirakata, T. Morita, K. Tanaka, J. Sato, Y. Morishita, M. Kanemaru, R. Kitamura, T. Shima, et al. A fully integrated 60-ghz cmos transceiver chipset based on wigig/ieee 802.11 ad with built-in self calibration for mobile usage. *IEEE Journal of Solid-State Circuits*, 48(12):3146–3159, 2013.
- [38] S. Shakib, M. Elkholly, J. Dunworth, V. Aparin, and K. Entesari. A wideband 28-ghz transmit–receive front-end for 5g handset phased arrays in 40-nm cmos. *IEEE Transactions on Microwave Theory and Techniques*, 67(7):2946–2963, 2019.
- [39] J. P. van Dijk, E. Kawakami, R. N. Schouten, M. Veldhorst, L. M. Vandersypen, M. Babaie, E. Charbon, and F. Sebastiano. Impact of classical control electronics on qubit fidelity. *Physical Review Applied*, 12(4):044054, 2019.
- [40] H. Wang, F. F. Dai, Z. Su, and Y. Wang. Sub-sampling direct rf-to-digital converter with 1024-apsk modulation for high throughput polar receiver. *IEEE Journal of Solid-State Circuits*, 55(4):1064–1076, 2020.
- [41] Q. Wu, W. Deng, H. Jia, H. Liu, S. Zhang, Z. Wang, and B. Chi. 8.1 an 11.5-to-14.3ghz 192.8dbc/Hz fom at 1mhz offset dual-core enhanced class-f vco with common-mode-noise self-cancellation and isolation technique. In *2023 IEEE International Solid-State Circuits Conference (ISSCC)*, pages 7–9, 2023.